

RESEARCH ARTICLE SUMMARY

X-INACTIVATION

Time-resolved structured illumination microscopy reveals key principles of Xist RNA spreading

Lisa Rodermund, Heather Coker, Roel Oldenkamp, Guifeng Wei, Joseph Bowness, Bramman Rajkumar, Tatyana Nesterova, David Miguel Susano Pinto, Lothar Schermelleh*, Neil Brockdorff*

INTRODUCTION: X chromosome inactivation (XCI) in mammals equalizes levels of X-linked gene expression in XX females relative to XY males. The XCI process is governed by the noncoding RNA Xist (X-inactive specific transcript), which is expressed from the inactive X chromosome, where it accumulates in cis and recruits factors required for chromatin-based gene silencing. The basis for cis-confinement to a single chromosome territory is poorly understood but is thought to involve interactions between specific Xist RNA binding proteins (RBPs)—for example, CIZ1 and SPEN—and a nuclear protein scaffold.

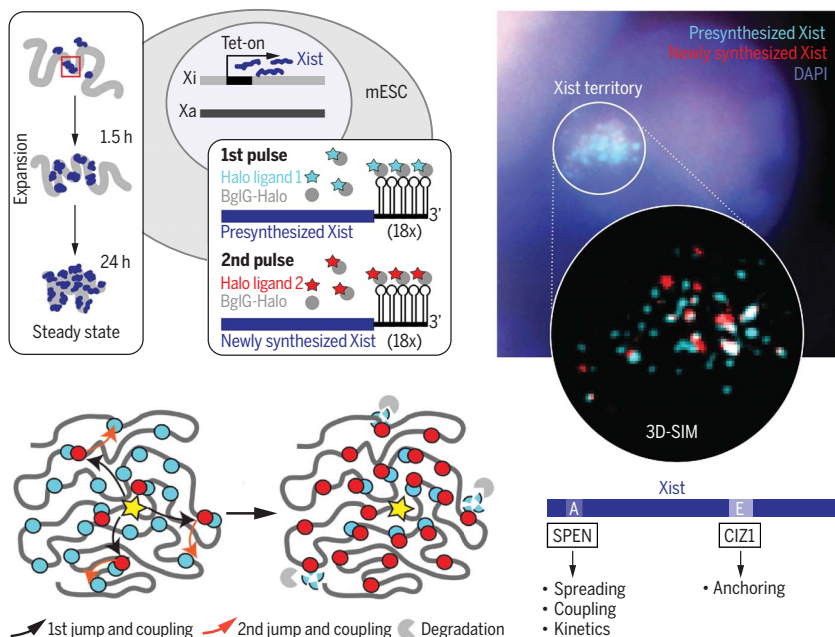
RATIONALE: To better understand the distinct and unusual behavior of Xist RNA, we developed RNA-SPLIT (sequential pulse locali-

zation imaging over time)—a method for time-resolved imaging of individual Xist molecules in the context of cells undergoing XCI. Here, we made use of the BglG/Bgl stem-loop system for tagging specific RNAs and a BglG-HaloTag fusion protein. Sequential pulsing with different fluorescent HaloTag ligands in living cells (mouse XX embryonic stem cells engineered with doxycycline-inducible Xist RNA) enabled us to image temporally resolved single Xist RNA molecules using super-resolution three-dimensional structured illumination microscopy (3D-SIM).

RESULTS: Consistent with previous work, we observed territories comprising around 50 to 100 single Xist molecules per cell. We identified a time window from 1.5 to 5 hours post-

induction, during which we could quantify a gradual increase of Xist molecules within the volume of the Xist territory, referred to as expansion phase. A later time point (24 hours postinduction) was taken as representative of Xist RNA behavior at steady state. The application of RNA-SPLIT allowed us to measure key parameters of Xist RNA dynamics in both phases. Xist molecules turned over approximately every 2 or 4 hours in expansion and steady state phases, respectively. Inhibition of Xist transcription by doxycycline washout resulted in a marked increase in Xist RNA stability, which suggests a feedback mechanism that balances rates of transcription and turnover. We observed a progressive radial enlargement of Xist RNA territories during expansion phase, with an estimated rate of $\sim 8 \mu\text{m}^3/\text{hour}$. Radial enlargement was not evident at steady state, which suggests that Xist RNA molecules localize in a more stochastic manner once X inactivation has been established. RNA-SPLIT further revealed that newly synthesized Xist molecules predominantly localize to sites where presynthesized molecules are present—a phenomenon we refer to as coupling. We extended our analysis to examine the effect of ablating CIZ1 and SPEN, factors implicated in the localization and cis-confinement of Xist RNA. Loss of function of CIZ1, which results in widespread nuclear dispersal of Xist RNA in differentiated cells, led to increased levels of transcription and increased stability of Xist RNA. In spite of widespread Xist RNA dispersal, coupling of pre- and newly synthesized Xist molecules was retained. SPEN loss of function led to major defects in the long-range localization of Xist RNA, reduced Xist RNA stability, and a disruption of Xist RNA coupling. The function of SPEN in Xist RNA behavior is genetically separable from its function in chromatin-based gene silencing in XCI.

CONCLUSION: The development of RNA-SPLIT has enabled quantitative spatial analysis of single Xist molecules over time during the establishment of XCI. Application of this methodology has revealed fundamental principles of Xist RNA behavior, including feedback control of Xist turnover and transcription, the kinetics of Xist RNA spreading, and the coupling of pre- and newly synthesized molecules. Beyond these insights, RNA-SPLIT has progressed our understanding of how the factors CIZ1 and SPEN affect different aspects of Xist RNA behavior and localization. ■



RNA-SPLIT enables functional analysis of Xist RNA localization and the role of associated RNA binding

proteins. Temporally distinct populations of Xist RNA molecules labeled in embryonic stem cell lines engineered with BglG stem-loop–tagged doxycycline-inducible Xist RNA and BglG-HaloTag fusion protein (top left). Unlike conventional widefield microscopy, visualization with super-resolution 3D-SIM imaging allows discrimination of individual Xist molecules transcribed at different time points (top right). This approach enabled quantification of the dynamic behavior of Xist RNA molecules characterized by “jump” and coupling (bottom left) and provided insights into functions of Xist-interacting proteins SPEN and CIZ1, which bind to A- and E-repeat domains of Xist RNA, respectively (bottom right). Tet-on, tetracycline-induced activation; Xi, inactive X chromosome; Xa, active X chromosome; mESC, mouse embryonic stem cell; DAPI, 4',6-diamidino-2-phenylindole.

The list of author affiliations is available in the full article online.

*Corresponding author. Email: neil.brockdorff@bioch.ox.ac.uk (N.B.); lothar.schermelleh@bioch.ox.ac.uk (L.S.)

Cite this article as L. Rodermund et al., *Science* 372, eabe7500 (2021). DOI: 10.1126/science.abe7500

READ THE FULL ARTICLE AT
<https://doi.org/10.1126/science.abe7500>

RESEARCH ARTICLE

X-INACTIVATION

Time-resolved structured illumination microscopy reveals key principles of Xist RNA spreading

Lisa Rodermund, Heather Coker, Roel Oldenkamp[†], Guifeng Wei, Joseph Bowness, Bramman Rajkumar, Tatyana Nesterova, David Miguel Susano Pinto, Lothar Schermelleh^{*}, Neil Brockdorff^{*}

X-inactive specific transcript (Xist) RNA directs the process of X chromosome inactivation in mammals by spreading in cis along the chromosome from which it is transcribed and recruiting chromatin modifiers to silence gene transcription. To elucidate mechanisms of Xist RNA cis-confinement, we established a sequential dual-color labeling, super-resolution imaging approach to trace individual Xist RNA molecules over time, which enabled us to define fundamental parameters of spreading. We demonstrate a feedback mechanism linking Xist RNA synthesis and degradation and an unexpected physical coupling between preceding and newly synthesized Xist RNA molecules. Additionally, we find that the protein SPEN, a key factor for Xist-mediated gene silencing, has a distinct function in Xist RNA localization, stability, and coupling behaviors. Our results provide insights toward understanding the distinct dynamic properties of Xist RNA.

X chromosome inactivation (XCI) is the mechanism that evolved in mammals to equalize levels of X-linked gene expression in XX females relative to XY males (1). The XCI process is controlled by a 17-kb-long noncoding RNA, Xist (X-inactive specific transcript), that functions in cis to silence the chromosome from which it is transcribed. Xist RNA localizes in cis across the length of the inactive X chromosome (Xi) elect, recruiting silencing factors that mediate chromatin modification and transcriptional inactivation of underlying genes (2). *Xist* transgenes expressed from ectopic autosomal locations recapitulate Xist RNA functions, including chromosome silencing in cis (3, 4).

A key challenge in X inactivation research is understanding the basis for cis-limited localization of Xist RNA. Early studies revealed that Xist RNA concentrates over chromosomal regions that have a high gene density (5) and that Xist RNA interacts tightly with the biochemically insoluble nuclear matrix fraction (6). Consistent with the latter observation, the nuclear matrix proteins hnRNPU and CIZ1 are required to anchor Xist RNA to the Xi territory (7–10). Related to these findings, super-resolution three-dimensional structured illumination microscopy (3D-SIM) imaging has revealed that Xist RNA molecules reside in distinct foci adjacent to hnRNPU in interchromatin channels that pervade the Xi territory (11). More recently, mapping of chromatin sites associated with Xist RNA using RNA

antisense purification sequencing (RAP-seq) (12) has revealed initial preferred localization to regions that are in close 3D proximity to the site of transcription, with subsequent spreading across the chromosome (13). These findings support the idea that preferred chromatin sites for Xist RNA association are not defined by their underlying DNA sequences.

Despite the aforementioned progress, our understanding of cis-limited localization of Xist RNA remains rudimentary. We recently proposed a model that suggests that the range over which Xist RNA spreads is a function of Xist RNA abundance, based on synthesis and degradation rates, and of the dynamics of the anchoring interaction of Xist ribonucleoprotein (RNP) particles with the insoluble nuclear matrix fraction (14). To test this hypothesis, we set out to quantify the dynamic behavior of Xist molecules. Previous studies have described approaches to fluorescently tag Xist RNA in living cells using fluorescent proteins (15, 16), but these systems are amenable only to conventional diffraction-limited fluorescence microscopy, which means that it is not possible to observe individual Xist molecules. To overcome this limitation, we developed a methodology tailored to measure the dynamics and localization of Xist molecules using super-resolution 3D-SIM, which we termed RNA-SPLIT (sequential pulse localization imaging over time). We use this approach to define critical parameters underpinning the behavior of Xist molecules and to show a previously unidentified role for the silencing protein SPEN in Xist RNA behavior.

Development of RNA-SPLIT to analyze Xist RNA dynamics

We set out to measure the dynamic behavior of individual Xist RNA molecules using super-

resolution 3D-SIM. The Bgl stem-loop system (17) was used for efficient labeling of inducible Xist RNA from its natural location on the X chromosome (Chr X) in XX female mouse embryonic stem cells (mESCs) or from an autosomal Xist transgene integration site on chromosome 15 (Chr 15) in XY male mESCs (Fig. 1A). The array of 18 Bgl stem-loops was inserted at the 3' end of Xist just after exon 7 (Fig. 1A). The Bgl stem-loops are tightly bound by the BglG protein, which was fused to a HaloTag in this instance (Fig. 1A). The use of HaloTag technology allowed for an increase in photostability and brightness sufficient for the application of 3D-SIM optical sectioning, which enabled the detection of distinct focal Xist signals within subnuclear regions in 3D space, referred to henceforth as Xist territories (Fig. 1B and movie S1). The intensity of fluorescent spots within Xist territories is approximately threefold higher than the unbound BglG-Halo signal in the nucleoplasm (fig. S1A). Insertion of the Bgl stem-loop array had no effect on Xist-mediated silencing, as determined using allelic chromatin RNA sequencing (ChrRNA-seq) (fig. S1B). Moreover, tagged Xist RNA was shown to recruit the known cofactor CIZ1 and to establish Xi-specific histone modifications (fig. S1C). Similar results were obtained for mESCs expressing the Chr 15 Xist transgene (fig. S1, D and E). Both cell lines showed clear Xist territories in >80% of cells 24 hours after doxycycline induction, and there was little to no detectable promoter leakiness (fig. S1F).

We identified a time window from 1.5 to 5 hours postinduction, during which we could quantify a gradual increase in the number of focal signals within the volume of the Xist territory (Fig. 1, C and D), referred to henceforth as the expansion phase. A later time point (24 hours) was taken as representative of Xist RNA behavior at steady state. The number of individual foci that we observed at 5 hours postinduction closely correlates with recent estimates for the number of Xist RNA molecules, 50 to 200 per cell (10, 11, 18), which indicates that each focal BglG-Halo signal corresponds to a single Xist RNA molecule. Further support for this conclusion is a notable pairwise colocalization of BglG-Halo foci and CIZ1 foci, the latter corresponding to CIZ1 protein bound to the Xist E-repeat, located immediately upstream of the Bgl stem-loop array (fig. S2, A to D).

We applied 3D-SIM live-cell imaging to detect distinct Xist foci over a period of 5 min using the fastest achievable frame rate (1 per 10 s) and found that the foci were largely static. A representative experiment is shown in fig. S2E and movie S2. One possibility is that translocation of Xist molecules from their site of transcription to relatively static binding sites is too rapid to capture with a frame rate

Department of Biochemistry, University of Oxford, Oxford OX1 3QU, UK.

^{*}Corresponding author. Email: neil.brockdorff@bioch.ox.ac.uk (N.B.); lothar.schermelleh@bioch.ox.ac.uk (L.S.)

[†]Present address: Division of Gene Regulation, Netherlands Cancer Institute, 1066 CX Amsterdam, Netherlands.

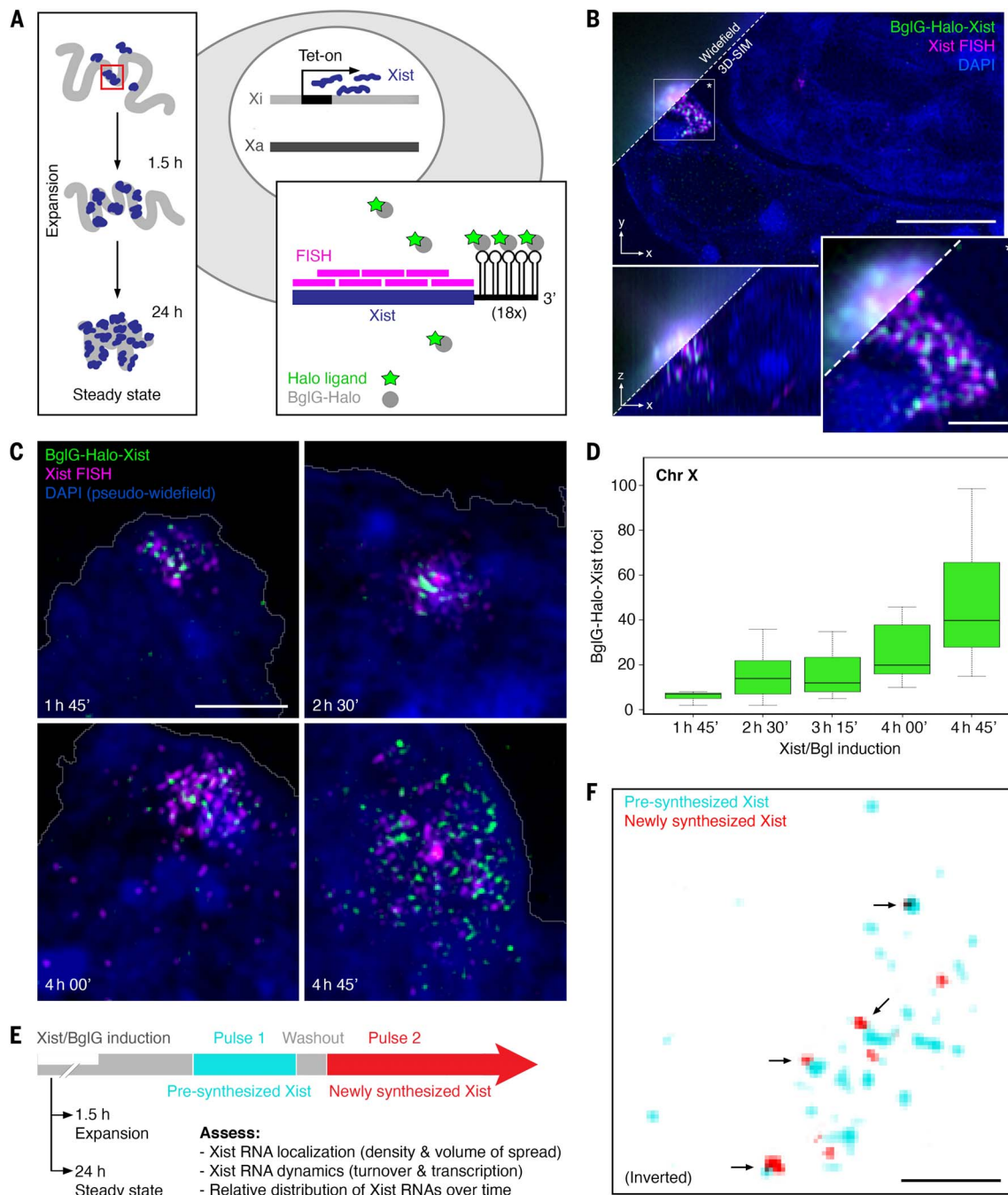


Fig. 1. Measuring Xist RNA behavior with RNA-SPLIT. (A) Schematic illustrating HaloTag labeling of Xist RNA in mESCs via the BglG/Bgl stem-loop system. Tet-on, tetracycline-induced activation. (B) Combined Xist RNA FISH with HaloTag staining of BglG-Halo-Xist visualized by 3D-SIM and conventional widefield microscopy for comparison. DNA is counterstained with DAPI (4',6-diamidino-2-phenylindole). Single cross section of a 3D image stack displayed in lateral and orthogonal view. Scale bars, 1 μ m. (C) Representative 3D-SIM images (z-projections) of Xist territories labeled by RNA FISH and HaloTag staining at different time points of Xist induction. Nuclear outlines are indicated in white. Scale bar, 2 μ m.

of 1 per 10 s. To address this possibility, we attempted single-particle tracking after photo-activation (PALM-SPT), but this was unsuccessful because it is not possible to discriminate RNA-bound and -unbound BglG-Halo fusion

proteins. Live-cell 3D-SIM imaging using slower frame rates was also not possible because of the extended motion of mESCs growing in colonies. To overcome this latter limitation, we developed RNA-SPLIT, in which successive

(D) Boxplots showing average number of focal Xist signals after Xist induction for different times determined from 3D-SIM analysis of Halo-BglG-labeled Xist molecules. $n = 11$ cells per time point. (E) Schematic illustrating the RNA-SPLIT regimen and the parameters of Xist RNA behavior measured in this study. (F) Representative 3D-SIM image (single cross section) of Xist RNA-SPLIT showing newly synthesized (red) and pre-synthesized (cyan) Xist molecules during expansion. Arrows indicate examples of newly synthesized Xist molecules closely associating with pre-synthesized Xist molecules. In this inverted representation, single pixels with similar cyan and red intensity display black. Scale bar, 1 μ m.

rounds of labeling with different HaloTag ligands performed in live cells allowed separate imaging of the first and the subsequent round of Xist RNA synthesis (henceforth referred to as pre-synthesized and newly synthesized Xist

RNA, respectively), analyzed with super-resolution 3D-SIM after formaldehyde fixation (Fig. 1, E and F). Exchange of the different BglG-ligand pairs on a single Xist molecule was found to be negligible (see experiments described below and supplementary text). Accordingly, varying labeling times in combination with a custom image processing and quantitative analysis pipeline enabled the measurement of various aspects of RNA dynamics and localization, notably density, spreading behavior,

RNA turnover, and transcription dynamics (Fig. 1E and fig. S3, A and B).

Chromosome context and rate of transcription modulate Xist RNA stability

We applied the RNA-SPLIT protocol to assess Xist RNA turnover after induction during expansion phase (after 1.5 hours) or steady state (after 24 hours) on both Chr X and Chr 15. A gradual reduction of presynthesized RNA was observed over a 4-hour time course,

with higher stability seen for Chr X-expressed compared with Chr 15-expressed Xist RNA (Fig. 2, A to C). In both cell lines, stability was higher in steady state compared with expansion phase. The latter observation indicates that, in addition to chromosome context effects, Xist RNA stability increases with XCI progression. We noted that turnover of pre-synthesized RNA is more evident toward the periphery of Xist territories (Fig. 2B). Results for Xist RNA turnover rates were validated

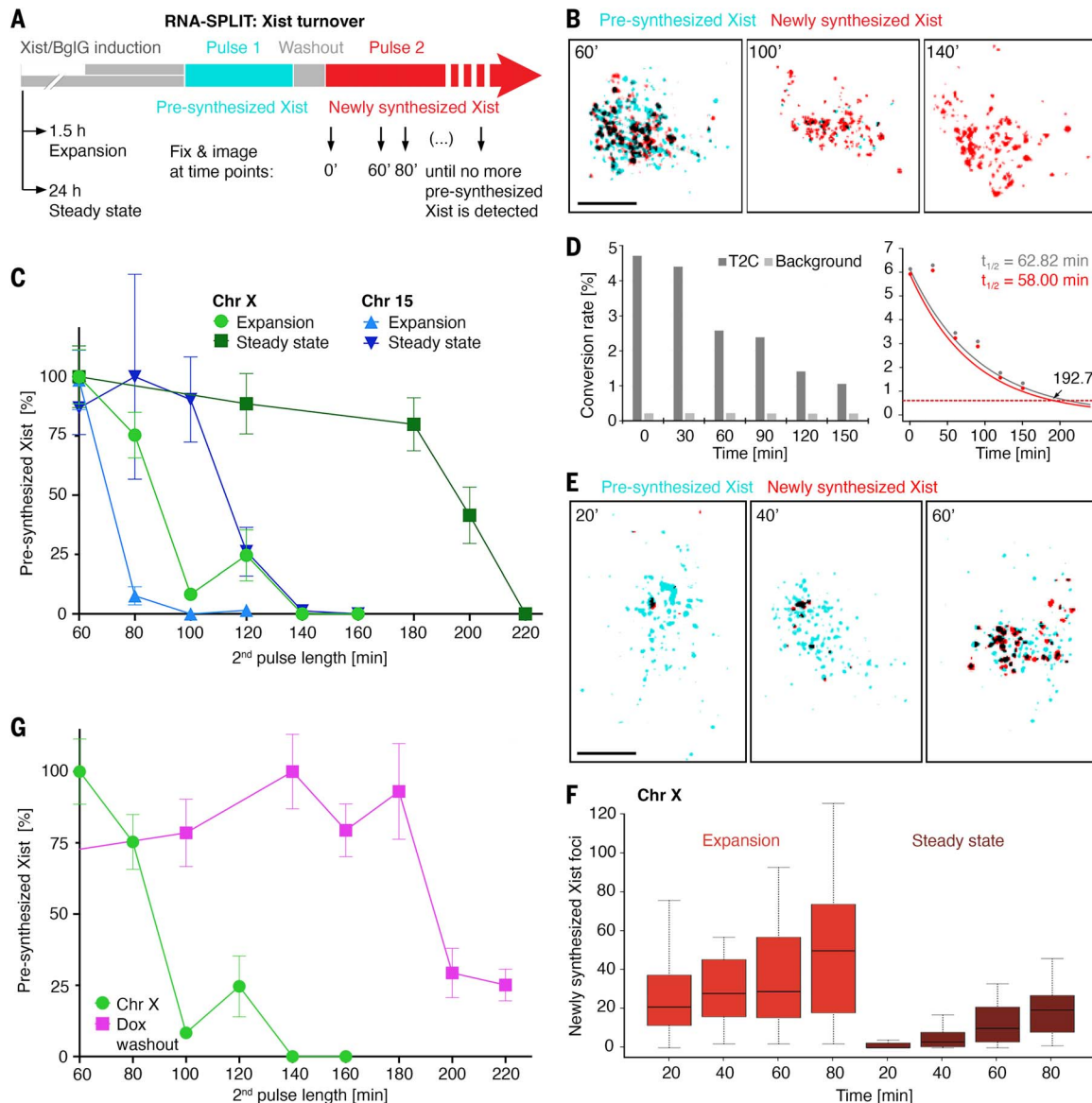


Fig. 2. Xist RNA stability is defined by its chromatin environment and rate of transcription. (A) Schematic illustrating RNA-SPLIT regimen to assess Xist RNA turnover. (B) Representative 3D-SIM images (z-projections; inverted representation) of RNA-SPLIT experiment to assess Xist molecule turnover during expansion. Note, presynthesized Xist molecules turn over more rapidly at the periphery of the territory. Scale bar, 2 μ m. (C) Plot showing quantification of Chr X and Chr 15 Xist RNA turnover during expansion and steady state. $n = 20$ cells per time point. (D) Plots of SLAM-seq experiments conducted during steady state showing decrease of thymine to cytosine (T2C) conversions over time (left) and data for Xist RNA (BglG-Halo-

tagged) replicates fitted to exponential decay curves (right) from which $t_{1/2}$ values are derived. The gray and red curves represent the raw T2C conversion and background-corrected conversion rates, respectively. The red dashed line indicates 10% of original signal. (E) Representative 3D-SIM images (z-projections) of Xist RNA on Chr X during expansion. Scale bar, 2 μ m. (F) Boxplots showing Xist RNA transcription over time during expansion and steady state phases. $n = 20$ cells per time point. (G) Plot showing effect of doxycycline (Dox) washout on turnover of Xist molecules during expansion. Presynthesized Xist counts were normalized by setting the highest count for each sample to 100%. $n = 20$ cells per time point.

using a different method, SLAM-seq [thiol(SH)-linked alkylation for the metabolic sequencing of RNA] (19) (Fig. 2D and fig. S4, A to C). SLAM-seq analysis further allowed us to ascertain that insertion of the Bgl stem-loop array does not substantially alter Xist transcript stability (fig. S4, A to C, and supplementary text).

Quantitation of the average number of Xist molecules in cells indicated a general decrease from expansion to steady state phase (fig. S4D), apparently at odds with the observed increase in stability. Further analysis revealed that this is accounted for by significantly elevated Xist transcription in expansion compared with steady state, as determined using RNA-SPLIT analysis of both Chr X- and Chr 15-expressed Xist RNA (Fig. 2, E and F, and fig. S4E). We noted increased transcription of Xist expressed in the Chr 15 compared with the Chr X context. These observations suggest that the abundance of Xist RNA may be regulated by a feedback mechanism that balances rates of synthesis and degradation.

A previous study reported increased Xist RNA stability after the inhibition of transcription by actinomycin D (15), which also points to a link between Xist RNA synthesis and turnover. Because actinomycin D treatment can lead to confounding indirect effects, we reexamined this finding using doxycycline washout in preference to terminate Xist expression. Doxycycline washout was performed 1.5 hours postinduction (fig. S4, F and G) and resulted in a marked increase in Xist RNA stability (Fig. 2G). This result further supports the existence of a promoter-independent feedback mechanism that links rates of Xist RNA transcription and turnover.

Time-resolved analysis of Xist RNA localization

We applied RNA-SPLIT to obtain temporally resolved 3D localization information at the level of individual Xist molecules in single cells. The site of Xist transcription was approximated on the basis of the density and fluorescence intensity of the newly synthesized Xist RNA signal. Using this approach, we found that the transcription site is, on average, located centrally within Xist territories in expansion phase and slightly more peripherally at steady state (fig. S5, A and B). More specifically, ~60% of estimated transcription sites were found in the inner zones during expansion (fig. S5B). In steady state, this was significantly reduced to ~40%, with ~60% of the transcription sites now found in the outer zone (fig. S5B). We went on to measure 3D distances of newly synthesized and presynthesized Xist RNA molecules from the transcription site (Fig. 3A). By dividing the Xist territory into three concentric zones, we were able to quantify the relative distribution of Xist molecules with respect to distance from

the transcription site over time (Fig. 3B). This analysis revealed that newly synthesized, but not presynthesized, Xist molecules spread in three dimensions from the transcription site toward the periphery of the Xist territory over a 1-hour time course during expansion phase. We calculated the average expansion rate to be $\sim 8 \mu\text{m}^3/\text{hour}$. Taking into account Xist RAP-seq data collected over a similar time course (13), as well as H2AK119ub1 chromatin immunoprecipitation sequencing (ChIP-seq) analysis described below, we infer that the observed spreading reflects Xist molecules being transported initially to sites in close proximity to the Xist locus (see also Discussion). 3D spread was not measurable using the same time course during steady state (Fig. 3B). Possible explanations include differences in Xist RNA turnover and transcription or a more-stochastic spread of Xist RNA as was proposed previously on the basis of RAP-seq and CHART-seq (capture hybridization analysis of RNA targets sequencing) experiments performed at later postinduction time points (13, 20).

Notably, RNA-SPLIT analysis revealed the frequent occurrence of pairwise association of presynthesized and newly synthesized Xist molecules (Fig. 3C, left panel), which we refer to as coupling. This phenomenon was also seen in experiments combining Xist RNA fluorescence in situ hybridization (FISH) with HaloTag staining, where HaloTag couplets are often observed over larger Xist RNA FISH foci (Fig. 3C, right panel).

We used nearest neighbor analysis (NNA) of 3D-SIM RNA-SPLIT images to quantify Xist RNP coupling at expansion and steady state in both Chr X and Chr 15 mESCs. Estimated median distances were in the range of 160 to 180 nm (Fig. 3D and fig. S6A). To determine the technical offset for colocalizing nuclear focal signals, we used 5-ethynyl-2'-deoxyuridine (EdU) pulse replication-labeled cells that were simultaneously detected with two colors (21). Taking into account the minimum resolvable separation using 3D-SIM of ~60 nm, which was obtained for the NNA of the dual-color EdU control sample (Fig. 3D), and an estimated diameter of Xist molecules of 50 nm [derived from the ratio of Xist RNA and ribosomal RNA (rRNA) length and the known size of a ribosome], these observations demonstrate very close spatial association of individual presynthesized and newly synthesized Xist molecules. This finding is further emphasized by comparison with a randomized NNA control (Fig. 3D and fig. S6A). Notably, there is no equivalent frequency of coupling of presynthesized with presynthesized or of newly synthesized with newly synthesized Xist molecules, which indicates that Xist molecules are not synthesized or transported as couplets, but rather come together at distant bound sites.

To rule out that the coupling effect is caused by binding of individual Xist molecules with the different HaloTag ligands, we performed a simultaneous dual-color labeling (fig. S6B). In this case, the majority of individual Xist molecules were either labeled with one or the other color (likely as a result of a limitation in both HaloTag labeling efficiency and capacity of stem-loop binding). A minority of foci showed precisely colocalizing signal for the two ligands. This is distinct from the coupling observed in RNA-SPLIT, where the two signals are spatially associated but separate. Accordingly, the distribution of measured NNA distances in the dual-labeling experiment is markedly different from that seen in RNA-SPLIT (fig. S6B and supplementary text).

Application of RNA-SPLIT to investigate the role of CIZ1 in Xist RNA behavior

To gain further insight into the mechanistic aspects of Xist RNA behavior, we applied RNA-SPLIT while perturbing factors known to be involved in cis-limited Xist RNA localization. First, we generated a knockout (KO) of the gene encoding CIZ1 (fig. S7, A to D), a protein associated with the insoluble nuclear matrix fraction, which interacts with Xist RNA and plays a pivotal role in anchoring Xist molecules in somatic cells (9, 10). In line with previous analyses (9, 10), we observed little or no effects on Xist RNA localization in undifferentiated mESCs (fig. S7, E and F). Accordingly, Xist transcript stability, transcription dynamics, and coupling were largely unaffected, and, moreover, Xist-mediated silencing determined using ChrRNA-seq was unaltered (fig. S8, A to E). In marked contrast, in differentiated neural precursor cells (NPCs) derived from the *Ciz1* KO mESCs, we observed a notable dispersal of Xist molecules throughout the entire nucleus (Fig. 4, A and B). We quantified the localization defect in NPCs by comparing intermolecule distances in *Ciz1* KO and wild-type (WT) NPCs (Fig. 4C). In WT NPCs, the density of Xist molecules increased (i.e., decreased distance between molecules) as differentiation progressed, whereas in *Ciz1* KO NPCs, density decreased (Fig. 4C).

Despite the observed delocalization of Xist RNA, ChrRNA-seq analysis demonstrated that there was no major difference in transcriptional silencing of the Xi (fig. S9A), consistent with the fact that *Ciz1* KO female mice are viable (9). Both RNA-SPLIT analysis and ChrRNA-seq demonstrated an increased Xist RNA molecule count in NPCs as compared with mESCs, with an even more notable increase in *Ciz1* KO NPCs (fig. S9, B and C). Further analysis by RNA-SPLIT revealed that this is linked to increased Xist transcription, most notably in *Ciz1* KO NPCs (fig. S9D). Additionally, Xist RNA stability is increased in NPCs compared

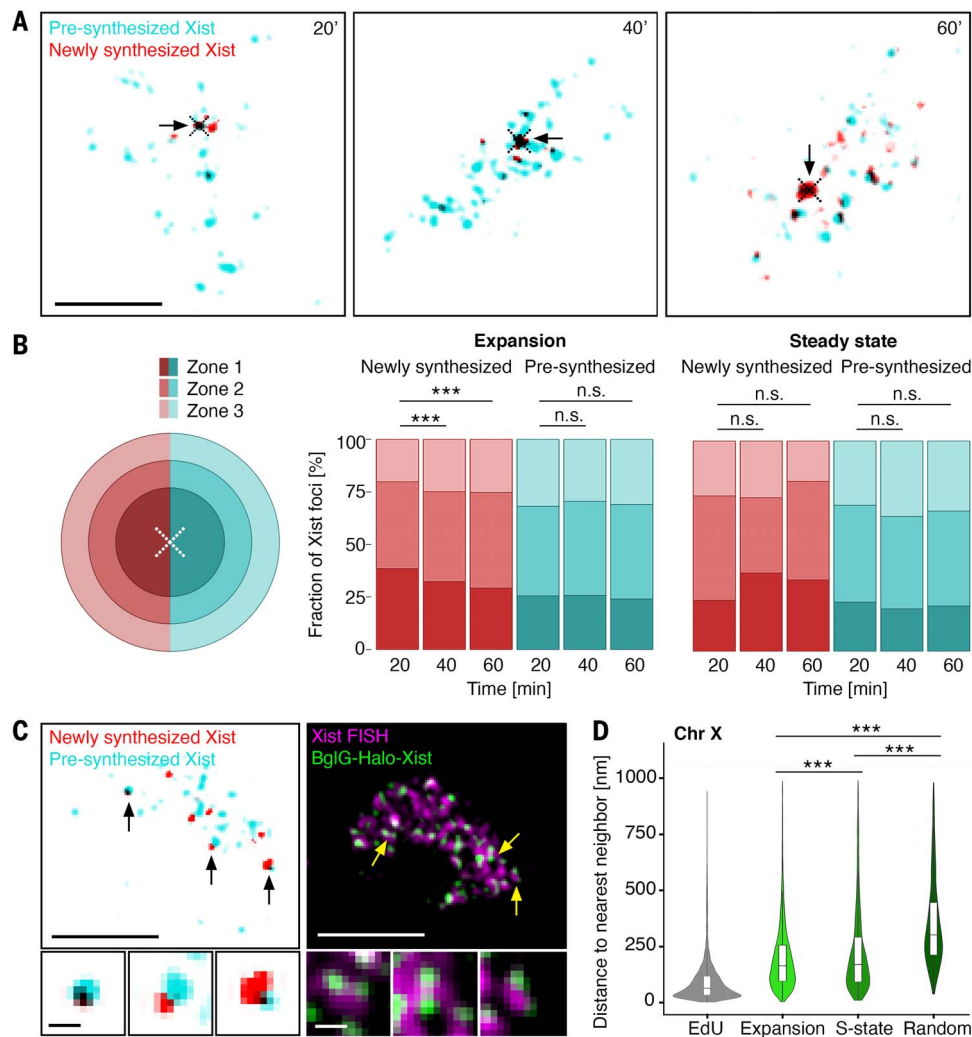


Fig. 3. Localization behavior of Xist molecules. (A) Representative 3D-SIM images (single z-section) of RNA-SPLIT illustrating spread of Xist molecules in expansion phase. Approximated Xist transcription site is indicated with black cross. Scale bar, 2 μ m. (B) Bar chart quantifying range of newly synthesized and presynthesized Xist molecules during expansion and steady state phases. Each signal was assigned to a zone, as illustrated in the schematic (left). $n = 40$ cells per time point. Significance was determined by unpaired two-sample Wilcoxon test ($***P < 0.0001$; n.s., not significant). (C) Representative 3D-SIM image (single

z-section) of RNA-SPLIT (left) and Xist RNA FISH combined with BglG HaloTag labeling (right) illustrating coupling of presynthesized and newly synthesized Xist molecules during expansion phase. Lower panels show examples of coupled Xist molecules. Selected couplets (arrows) are expanded in panels below. Scale bars, 2 μ m (main images) and 200 nm (lower panels). (D) Violin plots quantifying coupling of Xist molecules in expansion and steady state (S-state) phases. $n = 200$ cells per time point. Colocalization offset is defined using EdU control. Significance was determined by unpaired two-sample Wilcoxon test ($***P < 0.0001$).

with mESCs (fig. S9E). These observations indicate that the feedback mechanism linking Xist transcription and turnover is disrupted in *Ciz1* KO NPCs.

We went on to apply RNA-SPLIT to assess coupling of presynthesized and newly synthesized Xist molecules in NPCs. Coupling was readily observable in WT NPCs, which demonstrates that the phenomenon is common to both undifferentiated and differentiated cell types (Fig. 4D). Notably, we also observed coupling in *Ciz1* KO NPCs, despite the widespread dispersal of Xist molecules throughout the nucleus (Fig. 4E). This finding demonstrates that coupling of newly synthesized

and presynthesized Xist molecules is independent of cis-limited localization to the X chromosome.

A role for SPEN in Xist RNA localization

The protein SPEN, which binds to the A-repeat region of Xist RNA through a triple RRM domain, plays a central role in Xist-mediated gene silencing (8, 17, 22, 23). Silencing activity has been linked to a C-terminal SPOC domain that interacts with the NCoR-HDAC3 co-repressor complex (24–26). In recent work, we reported atypical Xist territories and reduced levels of Xist RNA resulting from SPEN loss of function (RRM deletion) and

similarly after deletion of the Xist A-repeat (27). Consistent with these observations, prior work reported that the A-repeat is critical for in cis localization of a truncated Xist RNA transgene (28). To further investigate a possible role for SPEN in Xist RNA localization, we engineered the SPEN RRM deletion in mESCs with endogenous inducible BglG-Halo-Xist (SPEN^{ΔRRM}; Fig. 5A and fig. S10A). Analysis by ChrRNA-seq confirmed a major silencing defect (fig. S10B), consistent with prior studies (26, 27). 3D-SIM combined with HaloTag staining revealed a visible defect in Xist RNA localization, both in expansion and steady state phases (Fig. 5B). This defect was also visible

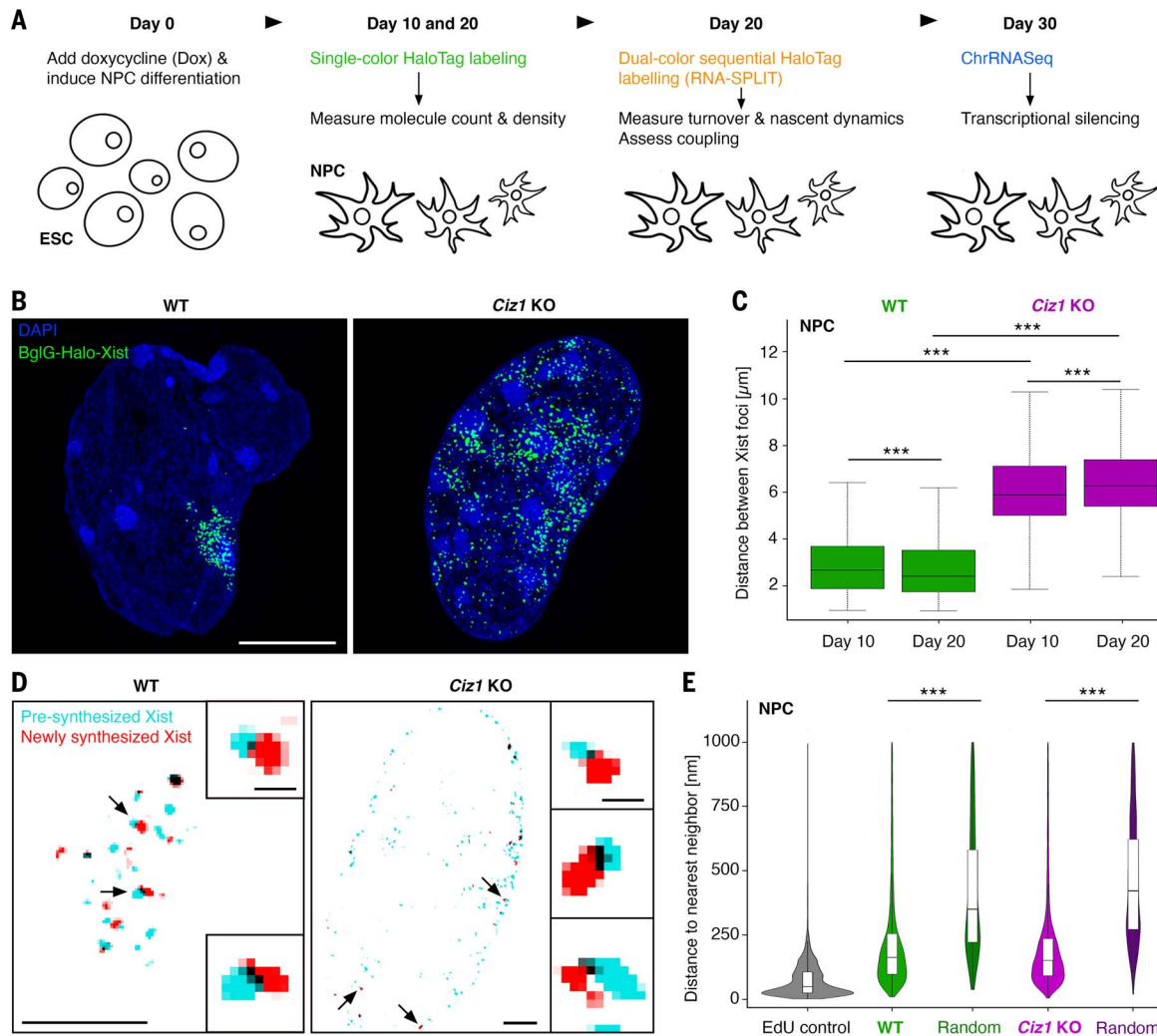


Fig. 4. Investigation of CIZ1 function in regulating Xist RNA behavior.

(A) Schematic illustrating differentiation of WT and *Ciz1* KO mESCs into NPCs. (B) Representative 3D-SIM images (z-projections) of Xist molecules in NPCs at day 10 of differentiation. Scale bar, 2 μm . (C) Boxplots representing density of Xist molecules in *Ciz1* KO NPCs. $n = 40$ cells per time point. Significance was determined using unpaired two-sample Wilcoxon test ($***P < 0.0001$). (D) Representative 3D-SIM images (single z-sections) of RNA-

SPLIT experiments for WT and *Ciz1* KO NPCs after 20 days of differentiation, showing coupling of presynthesized and newly synthesized Xist molecules. Selected couplings (arrows) are expanded in panels to the right. Scale bars, 2 μm (main images) and 200 nm (expanded images). (E) Corresponding NNA between Xist molecules in WT and *Ciz1* KO NPCs. $n = 150$ cells per time point. Significance was determined using unpaired two-sample Wilcoxon test ($***P < 0.0001$).

using Xist RNA FISH analysis and widefield microscopy (fig. S10C).

Prior studies have determined a close correlation of Xist-dependent Polycomb histone modifications and Xist RNA binding as determined by RAP (13), and we therefore carried out ChIP-seq analysis of Polycomb-mediated H2AK119ub1 to approximate the chromosomal distribution of Xist RNA in SPEN^{ARRM} mESCs. After induction of Xist for 3 or 24 hours—representing expansion and steady state, respectively—we observed a marked reduction in H2AK119ub1, in particular at sites further away from the *Xist* locus (Fig. 5C and fig. S10D). This observation indicates that SPEN is important for the long-range spread of Xist RNA.

Aberrant Xist RNA localization in SPEN^{ARRM} mESCs may be a consequence of abrogated gene silencing or, alternatively, may represent a distinct function of SPEN. To discriminate these possibilities, we generated mESCs with mutations in the SPOC domain (SPEN^{SPOCmut}), previously shown to disrupt interaction with the NCoR/HDAC3 co-repressor (29) (Fig. 5A). ChrRNA-seq analysis revealed that mutation of the SPEN SPOC domain abrogates Xist-mediated gene silencing, but to a lesser degree compared with the SPEN RRM deletion (fig. S10B). This observation is consistent with a recent study that analyzed a SPOC domain deletion mutant (26). Notably, aberrant localization of Xist RNA was less apparent in the SPEN^{SPOCmut} mESCs than in the SPEN^{ARRM}

mESCs, specifically during steady state (Fig. 5B), and moreover, there was little or no effect on Xist RNA distribution as assessed by ChIP-seq analysis of H2AK119ub1 (Fig. 5C and fig. S10D). These observations suggest a SPOC-independent function of SPEN in X inactivation that is linked to a role in Xist RNA localization.

SPEN modulates Xist RNA dynamics and is required for coupling Xist molecules

We went on to quantify the effect of SPEN mutations on Xist RNA behavior. The SPEN RRM deletion (and, to a lesser extent, mutation of the SPOC domain) resulted in a small decrease in the efficiency of Xist RNA induction (fig. S10C). Although the density of Xist

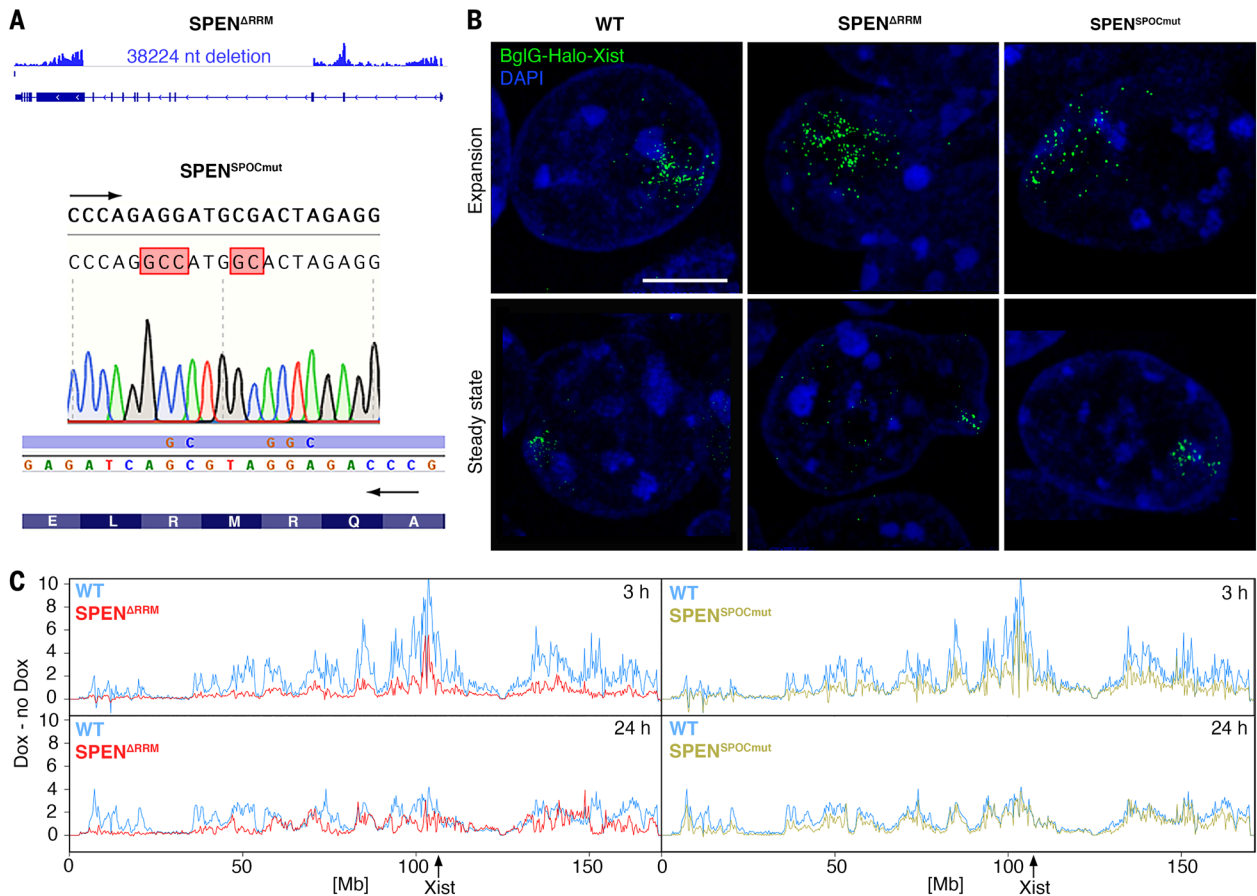


Fig. 5. A role for SPEN in Xist RNA localization. (A) UCSC genome browser screenshot with ChrRNA-seq track confirming 38,224-nucleotide deletion of sequences encoding the SPEN RRM region (top), with indication of nucleotide substitutions in the SPOC domain mutant confirmed by Sanger sequencing (bottom). (B) Representative 3D-SIM images (z-projections) showing Xist molecules within territories in WT and SPEN^{ΔRRM} mutant mESCs, as indicated in both expansion and steady state phases. Scale bar, 2 μm. (C) Plots showing gain of H2AK119ub1 within 250-kb windows on chromosome X determined by CHIP-seq analysis in SPEN^{ΔRRM} cells (left) and SPEN^{SPOCmut} cells (right) 3 hours (top) and 24 hours (bottom) after induction with doxycycline. The position of the Xist locus is indicated (arrow).

molecules was significantly decreased in both cell lines, the volume of spread was more affected in the SPEN RRM deletion (Fig. 6A and fig. S11A). Here, Xist occupied, on average, 70% of the nucleus in contrast to ~15% in the wild type (Fig. 6B). The SPEN RRM deletion (but not the SPOC domain mutant) leads to reduced levels of Xist RNA at steady state (fig. S11, B and C). This finding was not attributable to decreased Xist transcription, which was actually significantly increased both in expansion and steady state (Fig. 6C and fig. S11D), but rather to a significant decrease in Xist RNA stability (Fig. 6D).

In a final series of experiments, we applied RNA-SPLIT to determine whether SPEN mutations affect Xist RNP coupling. Although mutation of the SPOC domain had no apparent effect, deletion of the SPEN RRM significantly impaired coupling (Fig. 6, E and F, and fig. S11, E and F). Loss of coupling was evident in both expansion and steady state phases, although most markedly in the latter. Together, these results demonstrate a previously

unappreciated role for SPEN in Xist RNA behavior that is independent of gene-silencing functions mediated by the SPOC domain and likely involves regulation of the stability of Xist molecules, localization, and/or coupling.

Discussion

In this work, we identify two previously unrecognized parameters that need to be considered in modeling Xist RNA behavior. First, we find that the abundance of Xist molecules during expansion and steady state is maintained by a feedback mechanism that links rates of synthesis and degradation. Factors regulating the native Xist promoter are unlikely to be involved because our experiments analyzed Xist RNA expressed from the heterotypic doxycycline promoter. The feedback mechanism is unaffected by mutation of the SPEN SPOC domain, which indicates that it does not require Xist-mediated gene silencing, but it is perturbed upon SPEN RRM deletion and in *Ciz1* KO NPCs. Accordingly, we suggest that anchoring of Xist molecules to proteins of the

biochemically insoluble nuclear matrix fraction, which is perturbed in the absence of the SPEN RRM domain in mESCs and *Ciz1* KO NPCs, may be important for linking rates of transcription and turnover. Second, we find a distinct spatial colocalization of individual newly synthesized with presynthesized Xist molecules that we refer to as coupling. The spatial and temporal information we obtained indicates that coupling takes place at sites bound by Xist molecules rather than at the Xist transcription site. We speculate that a conformational switch occurs when Xist molecules anchor at destination sites and that this facilitates coupling, either with a mobile or diffusing Xist molecule or with a second anchored Xist molecule located at a different site but brought into proximity by elastic motion of mesoscale chromatin domains that subdivide the chromosome (30) (fig. S12, A and B).

Experiments to directly visualize the dynamic movement of single Xist molecules using live-cell 3D-SIM revealed a relatively

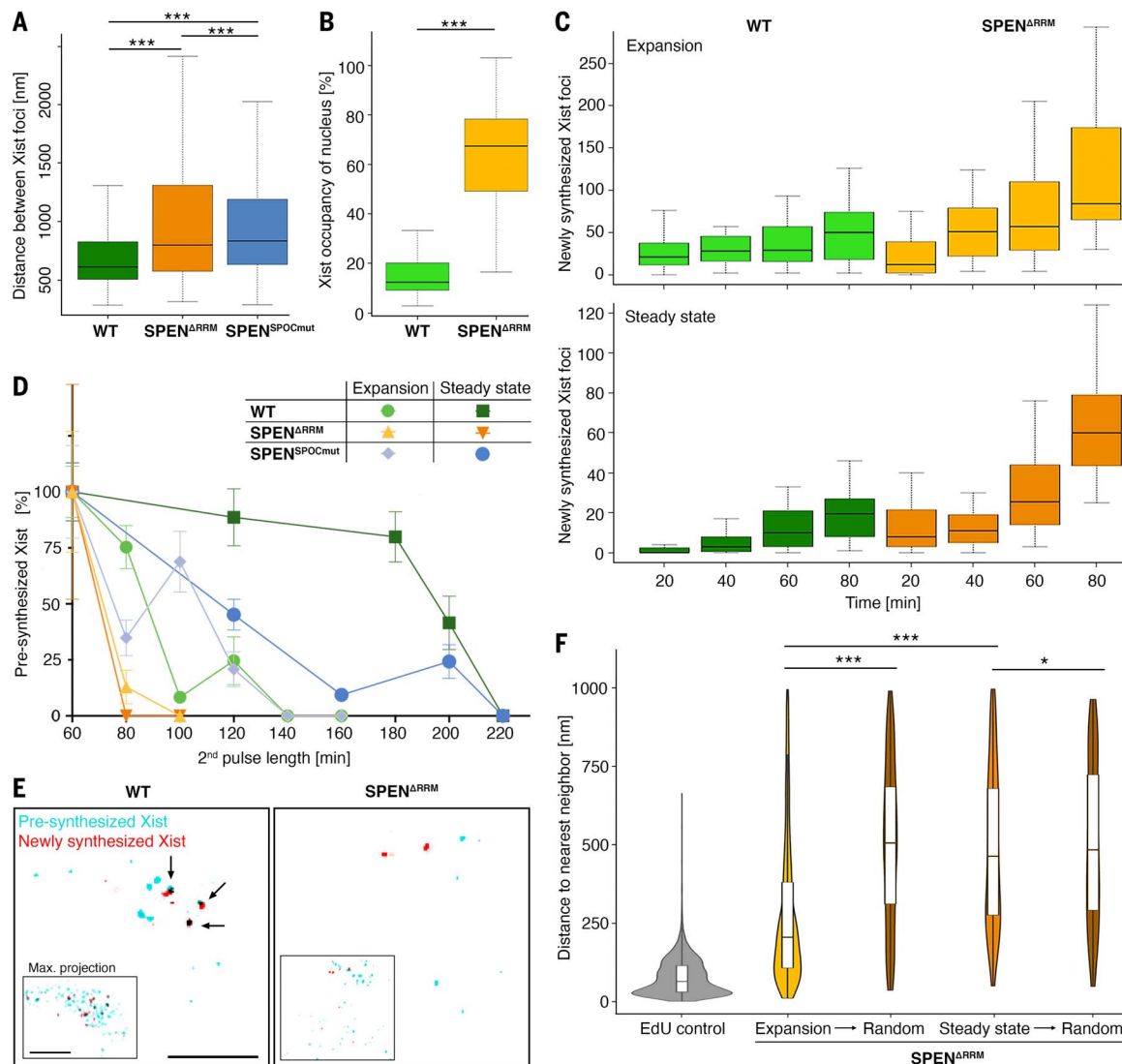


Fig. 6. SPEN modulates stability and coupling of Xist molecules. (A) Boxplots showing quantification of the density of Xist molecules in SPEN^{ARRM} and SPEN^{SPOCmut} cells. $n = 240$ cells per cell line. Significance was determined using unpaired two-sample Wilcoxon test ($***P < 0.0001$). (B) Boxplots showing Xist territory volume as proportion of nuclear volume in SPEN RRM deletion cells. $n = 120$ cells per cell line. Significance was determined using unpaired two-sample Wilcoxon test ($***P < 0.0001$). (C) Boxplots illustrating Xist RNA transcription in SPEN^{ARRM} mESCs during expansion and steady state. $n = 20$ cells

per time point. (D) Plot showing turnover of Xist molecules in mESCs during expansion and steady state as indicated. $n = 20$ cells per time point.

(E) Representative 3D-SIM images (single z-section) of RNA-SPLIT during steady state, illustrating abrogation of coupling of Xist molecules in SPEN^{ARRM} mESCs. Arrows indicate coupled Xist molecules. Insets show corresponding z-projections. Scale bars, 2 μm. (F) Violin plots showing abrogated coupling of Xist molecules in SPEN^{ARRM} mESCs. $n = 200$ cells per time point. Significance was determined using unpaired two-sample Wilcoxon test ($*P < 0.05$; $***P < 0.0001$).

static behavior, albeit subject to the limitations of the slow frame rate intrinsic to 3D-SIM imaging and the cell movements that occur using this experimental system. A similarly static behavior was observed in a recent study that used an alternative strategy for fluorescent labeling of Xist molecules for 3D-SIM imaging (18). This study additionally provided evidence that the static foci represent preferred anchor sites occupied by 50 to 100 Xist molecules in each cell. Regardless, it remains incontrovertible that Xist molecules must undergo dynamic movements to achieve their

distribution across the chromosome. Using RNA-SPLIT we determined that during the expansion phase, Xist territories enlarge radially at a rate of $\sim 8 \mu\text{m}^3/\text{hour}$. The behavior that we observe is consistent with the proposal that Xist molecules initially translocate to anchor sites that are proximal in three dimensions before being distributed more widely (13, 20). The fact that we see a relatively homogeneous and widespread distribution of the presynthesized Xist molecules during expansion, together with the observation that turnover appears to occur preferentially at the

periphery of Xist territories, suggests that individual Xist molecules translocate and couple at successive anchor sites in a series of “jumps” (fig. S12C). Although the basis for translocation of Xist molecules away from the Xist transcription site is unknown, we recently proposed that this could be attributable to fast diffusion of Xist molecules or to direct transfer through chromatin domain movements bringing preferred anchor sites and the Xist transcription site into direct contact—the Velcro ball model (14). Further investigation of this aspect of Xist RNA behavior will require

the development of approaches that enable individual Xist molecules to be tracked continually with a fast frame rate and/or over longer periods of time.

Our results demonstrate a key role for the silencing protein SPEN in long-range spreading of Xist RNA toward the chromosome termini. This previously unidentified function is independent of SPOC domain-mediated silencing activity and hence provides an explanation for differences observed previously when comparing SPEN null and SPOC domain mutant mESCs (26). Deletion of the Xist A-repeat, with which SPEN interacts, also results in disrupted spread of Xist RNA during expansion phase, as determined by RAP-seq analysis (13), and we suggest that this too is linked to the role of SPEN in Xist localization. It is possible that the SPOC-independent function of SPEN is important for transferring Xist RNA from initial 3D proximal sites to other locations on the chromosome. Although the underlying molecular mechanism for SPEN affecting Xist localization is unknown, our analysis of different mutations suggests a link to the abundance of Xist molecules and/or coupling. Further unraveling of this mechanism presents an important goal for future studies.

Materials and methods

Generation of cell lines

Tissue culture

Mouse embryonic stem cells (mESCs) were grown in Dulbecco's modified Eagle's medium (DMEM; Life Technologies) supplemented with 10% fetal calf serum (Seralab), 0.1 mM non-essential amino acids, 2 mM L-glutamine, 50 μ M β -mercaptoethanol and 100 U/ml penicillin/100 μ g/ml streptomycin (Life Technologies), as well as 1000 U/ml LIF (made in-house), on gelatin-coated plates with feeder cells, which were generated by inactivation of mouse fibroblasts with Mitomycin C (Sigma-Aldrich), at 37°C with 5% CO₂ in a humid atmosphere. Embryonic stem (ES) cells were passaged after treatment with TrypLE Express (Thermo Fisher Scientific) every 2 to 3 days. Before transfection, cells were grown on gelatin-coated 6-well plates with feeders.

WT mouse ES cell line

iXist-Chr X mESCs were used as parental cell line for the generation of the WT mESC line (27). The BglI stem-loop system was chosen for the labeling of Xist RNA. Due to concerns that BglI expression might be silenced over time, the BglI fusion protein was genetically engineered to be doxycycline inducible. Due to the superior fluorescent properties of organic dyes over fluorescent proteins and the possibility of flexible pulse labeling, a HaloTag approach was chosen for fluorescent labeling of the BglI protein for live-cell and super-resolution imaging (31). Cells were transfected

with 2 μ g of a vector encoding for doxycycline inducible BglI-Halo fusion protein using Lipofectamine 2000 (Life Technologies) according to the manufacturer's instructions. Cells were then passaged to 90 mm gelatin-coated Petri dishes with feeders and grown in medium containing 200 μ g/ml neomycin [Geneticin (G-418); Thermo Fisher Scientific] for 10 days. Clones were picked and genomic DNA (gDNA) was extracted, before successful insertions were screened by polymerase chain reaction (PCR) (table S1). Selected clones were expanded, and BglI-Halo expression was assessed by HaloTag ligand staining and subsequent wide-field fluorescence microscopy with an inverted fluorescence Axio Observer Z.1 microscope (Zeiss). Having selected a clone with intermediate BglI expression, low enough to minimize background but high enough to label all Xist molecules efficiently, a BglI stem-loop array was inserted within exon 7 of the *Xist* locus by CRISPR-Cas9-mediated genome engineering. Here, a homology construct containing homology regions 1 kb 5' and 3' of the targeted insertion site within exon 7 of *Xist* was targeted by cotransfection with a specific single guide RNA (sgRNA) (table S1), which was designed using the WGE - CRISPR design tool (Wellcome Sanger Institute) and cloned into a backbone vector encoding for the CRISPR-Cas9 protein (PX459, Addgene). Cells were transfected overnight with 2 μ g of the sgRNA construct and 1.15 μ g of the targeting construct using Lipofectamine 2000 (Life Technologies) according to the manufacturer's instructions, and then passaged to 90 mm gelatinized Petri dishes with feeders. Cells were grown under antibiotic selection with 1.75 μ g/ml puromycin for 48 hours and thereafter grown for a further 9 days before being picked. Clones with successful insertion were selected by PCR screening after gDNA extraction (table S1). Successful labeling of BglI-Halo-Xist was confirmed by HaloTag ligand staining followed by 3D-SIM. Comparison of BglI-Halo-Xist signal intensity to background signal from unbound BglI-Halo allowed for the selection of the most suitable cell line for imaging experiments.

Transgenic mouse ES cell line

XY P4D7 mESCs were used as parental cell line for the generation of the transgenic mESC line (17). A construct with doxycycline inducible Xist containing an array of 18 BglI stem-loops within exon 7 was used (17). Additionally, cells were transfected with the construct encoding doxycycline inducible BglI-Halo protein described earlier. Cells were cotransfected overnight with 5 μ g of the transgenic Xist and 2.5 μ g of the BglI-Halo construct using TransIT-LT1 transfection reagent (Mirusbio) according to the manufacturer's instructions. Cells were then passaged to 90 mm gelatin-coated Petri

dishes with feeders and grown in medium containing 200 μ g/ml neomycin (Geneticin (G-418); Thermo Fisher Scientific) for 10 days. Successful insertions of the BglI-Halo sequence were screened by PCR analysis of the gDNA (table S1). Transgenic Xist expression was assessed by Xist RNA FISH and subsequent widefield fluorescence microscopy with an inverted fluorescence Axio Observer Z.1 microscope (Zeiss). BglI-Halo expression and efficient labeling of transgenic BglI-Halo-Xist was confirmed by HaloTag ligand staining and 3D-SIM. Comparison of BglI-Halo-Xist signal intensity to background signal from unbound BglI-Halo allowed for the selection of the most suitable cell line for imaging experiments. ChrRNA-seq later enabled determination of the insertion site of transgenic Xist on chromosome 15.

Ciz1 KO ES cell line

The aforementioned WT ES cell line was used as parental cell line for the generation of the *Ciz1* KO mESCs by CRISPR-Cas9-mediated genome engineering. Here, a sgRNA, which had been previously used to induce a frameshift mutation (10), was used in combination with a second sgRNA designed using the WGE - CRISPR design tool to achieve a genomic deletion of 10.66 kb, resulting in the deletion of most of the *Ciz1* gene (table S1). The sgRNAs were cloned into backbone vectors encoding for the CRISPR-Cas9 protein (PX459, Addgene). Cells were transfected overnight with 2 μ g of each sgRNA construct using Lipofectamine 2000 (Life Technologies) according to the manufacturer's instructions. Cells were then passaged to 90 mm gelatinized Petri dishes with feeders and grown under antibiotic selection with 2 μ g/ml puromycin for 48 hours. Colonies were grown for 8 days before being picked. Selected clones with successful genomic deletion were screened for by PCR analysis of gDNA (table S1). Absence of *CIZ1* was confirmed by Western blot and immunofluorescence staining for *CIZ1*, and successful labeling of BglI-Halo-Xist was confirmed by HaloTag ligand staining followed by 3D-SIM. A final clone for analysis was chosen on the basis of the results of these assays, as well as the comparison of BglI-Halo-Xist signal intensity to background signal from unbound BglI-Halo.

SPEN^{ARRM} ES cell line

The aforementioned WT ES cell line was used as parental cell line for the generation of the SPEN^{ARRM} mESCs by CRISPR-Cas9-mediated genome engineering. Previously described sgRNAs (23) were used to achieve a genomic deletion of 38 kb, resulting in the KO of RRM2-4 of *Spn* (table S1). Cells were transfected and successful deletion was screened for as described above for the *Ciz1* KO cell line. SPEN RRM deletion in selected clones was

confirmed by Southern blot. Presence of polyploid and XO cells was excluded by Xist RNA FISH and successful labeling of BglG-Halo-Xist was confirmed by HaloTag ligand staining followed by 3D-SIM. A final clone for analysis was chosen on the basis of the results of these assays, as well as the comparison of BglG-Halo-Xist signal intensity to background signal from unbound BglG-Halo.

SPEN^{SPOCmut} ES cell line

The aforementioned WT ES cell line was used as parental cell line for the generation of the SPEN^{SPOCmut} mESCs by CRISPR-Cas9-mediated genome engineering. The SPOC mutant, which disrupts the interaction between SPEN and NCoR/SMRT complex (32), was achieved by amino acid substitutions R3552A and R3554A in the SPOC domain of SPEN. This substitution was previously described to abolish binding of SPEN to NCoR1 an SMRT co-repressive complexes in vitro (29). The substitutions were engineered into a 0.5 kb homology construct corresponding to the region of SPEN exon 14. The sgRNA (table S1) was cloned into a backbone vector encoding for the CRISPR-Cas9 protein (PX459, Addgene). Cells were transfected overnight with 1.42 µg of the sgRNA construct and 2.5 µg of the targeting construct using Lipofectamine 2000 (Life Technologies) according to the manufacturer's instructions. Cells were then passaged to 90 mm gelatinized Petri dishes with feeders and grown under antibiotic selection with 3 µg/ml puromycin for 48 hours. Colonies were grown for 10 days before being picked. Selected clones with successful amino acid substitution were screened after gDNA extraction by NcoI digestion, PCR analysis, and Sanger sequencing of the PCR fragments (table S1). Presence of polyploid and XO cells was excluded by Xist RNA FISH and successful labeling of BglG-Halo-Xist was confirmed by HaloTag ligand staining followed by 3D-SIM. Chromatin RNA sequencing (ChrRNA-seq) finally confirmed successful amino acid substitution and a final clone for analysis was chosen on the basis of the cumulative results of these assays, as well as the comparison of BglG-Halo-Xist signal intensity to background signal from unbound BglG-Halo.

NPC derivation

To study Xist behavior in differentiated cells, WT and *Ciz1* KO mESCs were differentiated into neural progenitor cells (NPCs) following a previously adapted protocol (33, 34). Cells were grown in gelatin-coated T25 flasks with feeder cells. Feeders were removed before differentiation by preplating three times for 40 min each. Then, 0.45×10^6 cells and 0.55×10^6 cells, respectively, were plated in a gelatin-coated T25 flasks each and grown in N2B27 medium containing 1 µg/ml doxycycline for 7 days. On day 7, the flasks were treated

with Accutase (Millipore) and 3×10^6 cells each were plated in each 90 mm bacterial petri dishes with N2B27 medium containing 1 µg/ml doxycycline and 10 ng/ml EGF and FGF (Peprotech) to prevent cellular attachment. For imaging at day 10 of differentiation, cells were plated onto gelatin-coated 18x18 mm No. 1.5H precision coverslips (± 5 µm tol.; Marienfeld Superior) at day 7. At day 10, cell aggregates were collected by mild centrifugation, before being plated onto gelatin-coated 90 mm petri dishes in N2B27 medium containing 1 µg/ml doxycycline and 10 ng/ml EGF and FGF (Peprotech) each. When ~80% confluent, cells were split 1:4 by Accutase (Millipore) treatment at room temperature followed by collection in PBS and centrifugation at 1500 rpm for 5 min. For HaloTag staining at day 20 of differentiation, cells were plated onto precision coverslips at day 16 of differentiation. For ChrRNA-seq at day 30 of differentiation, cells were expanded onto one 145 mm petri dish per replica on day 25 of differentiation.

Xist RNA FISH

Xist RNA FISH for scoring

All cells were grown on gelatin-coated 18x18 mm No. 1.5H precision coverslips (± 5 µm tol.; Marienfeld Superior) in a 6-well plate on a layer of feeder cells. When reaching 60 to 70% confluency, mESCs were induced for 3 hours or 24 hours with 1 µg/ml doxycycline, reserving one coverslip per experiment without doxycycline induction. After induction, coverslips were washed briefly with PBS twice, before being fixed with 3.7% formaldehyde in PBS at room temperature for 10 min. Cells were rinsed with PBS and then permeabilized with 0.5% Triton X-100 in PBS for 10 min at room temperature, followed by two washes with 70% EtOH. Coverslips were then dehydrated with subsequent washes with 80%, 95%, 100% EtOH for 5 min each, and dried briefly. Each coverslip was hybridized with 15 µl probe/ hybridization buffer mix. Xist probe was generated from an 18 kb cloned cDNA spanning the whole Xist transcript using a nick translation kit (Abbott Molecular) as previously described (17). 3 µl Texas Red labeled Xist RNA FISH probe per hybridization was added to 1/3 volume 10 mg/ml salmon sperm DNA, then precipitated by addition of 1/10 volume of 3 M NaOAc and 3 volumes 100% EtOH. After washing with 70% EtOH, the pellet was dried by speed vacuum and resuspended in 6 µl deionized formamide (Sigma) per hybridization. An equal amount of 2x hybridization buffer [4x SSC, 20% dextran sulfate, 2 mg/ml BSA (NEB), 1/10 volume nuclease free water and 1/10 volume VRC prewarmed at 65°C for 5 min before use] was added, and the probe/hybridization buffer mix was denatured at 75°C for 5 min before being chilled on ice and used for hybridization in a humid cham-

ber overnight at 37°C. The next day, coverslips were washed three times with prewarmed 50% formamide/2x SSC at 42°C for 5 min each, and subsequently three times with 2x SSC at 42°C for 5 min each. Coverslips were mounted with 4',6-diamidino-2-phenylindole (DAPI) containing Vectashield antifade mounting medium (Vector Labs) centrally on Superfrost Plus microscopy slides (VWR). Slides were dried, sealed using clear nail polish, and cleaned for imaging. Imaging and scoring were carried out using an inverted fluorescence Axio Observer Z.1 microscope (Zeiss) using a PlanApo $\times 63/1.4$ NA oil-immersion objective. Images were acquired using AxioVision software.

Xist RNA FISH for 3D-SIM

This protocol was adapted from the Stellaris FISH protocol (Biosearch Technologies) for a combination of Xist RNA FISH with HaloTag ligand staining of BglG-Halo-Xist. All cells were grown on gelatin-coated 18x18 mm No. 1.5H precision coverslips in a 6-well plate on a layer of feeder cells. When reaching 60 to 70% confluency, mESCs were induced for 3 hours or 24 hours with 1 µg/ml doxycycline, before being stained with HaloTag ligand. After washout of the ligand, coverslips were washed twice with PBS and fixation was carried out by adding 3% formaldehyde (pH 7) prepared in fresh PBS for 10 min at room temperature. A stepwise exchange of PBST (0.05% Tween 20 PBS) was carried out, then coverslips were washed twice in PBST. Cells were permeabilized in 0.2% Triton X-100 PBS for 10 min at room temperature, before being washed twice with PBST. Then, coverslips were blocked in 2% BSA / 0.5% fish skin gelatin / PBST containing freshly added RNasin Plus (Promega) at a final concentration of 2 U/µl for 30 min. In the meantime, the Xist RNA FISH probe was prepared and precipitated as described before. However, after speed vacuum the probe pellet was resuspended in 12 µl Stellaris Hybridization buffer (Biosearch Technologies) per hybridization instead of formamide. The probe/hybridization buffer was prepared as described above, with the exception that the 2x hybridization buffer was prepared with 1/10 volume formamide before being added to the probe. After blocking, the cells were washed three times with PBST and fixed as before. Then, the coverslips were washed twice in PBST again, followed by a wash in 2x SSC. Next, the coverslips were incubated with FISH probe/hybridization buffer overnight at 37°C on parafilm in an extra humid chamber. The next day, the coverslips were transferred to a 6-well plate containing 1 ml wash buffer A (Biosearch Technologies) per well. After an incubation at 37°C for 30 min, wash buffer A was replaced with 1 ml wash buffer A containing 5 ng/ml DAPI, and coverslips were incubated at 37°C for 30 min. 1 mL of 2x SSC was added to each

well, followed by an incubation of 5 min at room temperature. Finally, coverslips were mounted centrally on the unfrosted side of Superfrost Plus microscopy slides (VWR) using nonsetting Vectashield antifade mounting medium (without DAPI), sealed with clear nail polish and imaged within a week using the DeltaVision OMX V3 Blaze system (GE Healthcare).

Immunofluorescence labeling

All cells were grown on gelatin-coated 18x18 mm No. 1.5H precision coverslips in a 6-well plate on feeder cells. When reaching 60 to 70% confluency, mESCs were induced for 3 hours or 24 hours with 1 $\mu\text{g}/\text{ml}$ doxycycline. Optionally, cells were stained with HaloTag ligand at this stage for a combination of HaloTag ligand and immunofluorescence staining. Coverslips were washed twice with PBS and fixation was carried out by adding 2% formaldehyde prepared in fresh PBS (pH 7) for 10 min at room temperature. A stepwise exchange of PBST was carried out, before coverslips were washed twice in PBS. Then, cells were permeabilized with 0.2% Triton X-100 in PBS for 10 min at room temperature, followed by a wash with PBST. Coverslips were blocked using 3% BSA/ 5% normal goat serum/ PBST on parafilm in a humid chamber for 30 min at room temperature, and then incubated with primary antibody (table S2) diluted in block buffer for 1 hour in a humidified chamber at 37°C. After three washes in PBST, coverslips were incubated with the Alexa Fluor-conjugated secondary antibody (table S2) diluted 1:1000 in block buffer for 30 min in a humidified chamber at 37°C. After another 4 washes with PBST, the cells were post-fixed as before, followed by a final wash in PBST. Lastly, coverslips were incubated with 2 $\mu\text{g}/\text{ml}$ DAPI in PBS for 10 min, before being mounted in non-setting Vectashield medium centrally on the unfrosted side of Superfrost Plus microscopy slides (VWR), sealed with clear nail polish, and imaged within a week using the DeltaVision OMX V3 Blaze system (GE Healthcare).

HaloTag staining

All cells were grown on gelatin-coated 18x18 mm No. 1.5H precision coverslips in a 6-well plate on feeder cells. When reaching 60 to 70% confluency, mESCs were induced for 3 or 24 hours with 1 $\mu\text{g}/\text{ml}$ doxycycline. Then, cells were incubated with 50 nM diAcFAM HaloTag ligand (488 nm, Promega) and 1 $\mu\text{g}/\text{ml}$ doxycycline for 45 min, before being washed with medium containing 1 $\mu\text{g}/\text{ml}$ doxycycline for 15 min. After a brief wash with PBS, cells were fixed for 10 min at room temperature with 2% formaldehyde prepared fresh in PBS (pH 7). A stepwise exchange of PBST was carried out, and cells were permeabilized with 0.2% Triton

X-100 for 10 min, followed by two washes with PBST. Next, cells were incubated with 2 $\mu\text{g}/\text{ml}$ DAPI in PBST for 10 min, before being washed briefly with PBS and, subsequently with ddH₂O to remove salt. Lastly, coverslips were mounted on the unfrosted side of Superfrost Plus microscopy slides (VWR) using nonsetting Vectashield medium, sealed with clear nail polish and imaged within a week using the DeltaVision OMX V3 Blaze system (GE Healthcare).

3D-SIM

Acquisition

3D-SIM imaging was performed on a DeltaVision OMX V3 Blaze system (GE Healthcare) equipped with a 60x/1.42 NA Plan Apo oil immersion objective (Olympus), pco.edge 5.5 sCMOS cameras (PCO), and 405, 488, 593, and 640 nm lasers. Image stacks were acquired with a z-distance of 125 nm and with 15 raw images per plane (5 phases, 3 angles). Spherical aberration after reconstruction was reduced by using immersion oil of different refractive indices (RIs) matched to respective optical transfer functions (OTFs). Here, immersion oil with an RI of 1.514 was used for the sample acquisition and matched to OTFs generated using immersion oil of RI 1.512 for the blue and green, and 1.514 for the red channel. OTFs were acquired using 170 nm diameter blue emitting PS-Speck beads and 100 nm diameter green and red emitting FluoSphere beads (Thermo Fisher Scientific).

Reconstruction

The raw data were computationally reconstructed with softWoRx 6.5.2 (GE Healthcare) using channel-specific OTFs and Wiener filter settings of 0.005. A lateral (x-y) resolution of ~120 nm and an axial (z) resolution of ~320 nm was achieved (30). All data underwent assessment via SIMcheck (35) to determine image quality via analysis of modulation contrast to noise ratio (MCNR), spherical aberration mismatch, reconstructed Fourier plot, and reconstructed intensity histogram values. Of note, DAPI reconstructions in mESC were typically below the quality threshold levels of average MCNR of 5, and were therefore only used to indicate the nuclear outlines. Reconstructed 32-bit 3D-SIM datasets were thresholded to the stack modal intensity value and converted to 16-bit composite z-stacks to discard negative intensity values using SIMcheck's "threshold and 16-bit conversion" utility and MCNR maps were generated using the "raw data modulation contrast" tool of SIMcheck. To eliminate false positive signals from reconstructed noise, we applied a modulation contrast filtering using an adapted in-house Fiji script (36). Here, all pixels in the reconstructed dataset where the corresponding MCNR values in the raw data map fall below an empirically chosen threshold of 4.0 are set

to zero intensity. Thereafter, the resulting "masked" reconstructed dataset is blurred with a Gaussian filter with 0.8-pixel radius (xy) to smoothen hard edges (fig. S3B; the "modulation contrast filter" script has meanwhile been implemented as utility with added functionalities in an updated version of SIMcheck). Widefield images were generated from averaging phase shifted raw 3D-SIM data of each z-position. Iterative deconvolution of widefield image stacks was performed in softWoRx using standard settings.

Alignment

Color channels were registered in 3D with the open-source software Chromagnon 0.85 (37) determining alignment parameter (x,y,z-translation, x,y,z-magnification, and z-rotation) from a 3D-SIM dataset acquired on the date of image acquisition of multicolor-detected 5-ethenyl-2'-deoxyuridine (EdU) pulse replication labeled C127 mouse cells serving as biological 3D alignment calibration sample (21).

3D-SIM live-cell imaging

Cells were grown on gelatin-coated 35 mm No. 1.5H glass bottom imaging dishes (Ibidi) on feeder cells. When reaching 50% confluency, mESCs were induced for 24 hours with 1 $\mu\text{g}/\text{ml}$ doxycycline. Then, cells were incubated with medium containing 50 nM JF-646 HaloTag ligand (Janelia Fluor 646, kindly provided by Luke Lavis, HHMI Janelia) and 1 $\mu\text{g}/\text{ml}$ doxycycline for 45 min, before being washed with medium containing 1 $\mu\text{g}/\text{ml}$ doxycycline for 15 min. Before imaging, cells were washed briefly with PBS and medium was replaced with phenol red free medium with 1 $\mu\text{g}/\text{ml}$ doxycycline. For live-cell 3D-SIM, image stacks were acquired in 10-s intervals for up to 10 min. Image acquisition was performed at 37°C with 5% CO₂. To adapt for the temperature increase, immersion oil with an RI of 1.520 was used for the sample acquisition and matched to OTFs generated. Images were then processed as described above, with the exception that bleach correction was carried out.

RNA-SPLIT

Sample preparation

All cells were grown on gelatin-coated 18x18 mm No 1.5H precision coverslips as described above for HaloTag staining. ES cells were induced for different times with 1 $\mu\text{g}/\text{ml}$ doxycycline and stained with HaloTag ligands dependent on the variation of RNA-SPLIT as described below. RNA-SPLIT was determined to achieve optimal results when using the diAcFAM HaloTag ligand (Promega) as first pulse label and the JF-585 HaloTag ligand (kindly provided by Luke Lavis, HHMI Janelia) as second pulse label. Initial experiments with different dye concentrations showed that a concentration of 50 nM for each of the ligands

yielded optimal results. After a wash with PBS, samples were fixed and mounted as described above.

Nascent Xist RNA dynamics

For assessing the transcription dynamics of Xist RNA, cells grown on precision coverslips were sequentially stained with two different HaloTag ligands in each experiment. For analysis of expansion or steady state phase, cells were induced for either 1.5 or 24 hours with 1 $\mu\text{g}/\text{ml}$ doxycycline, respectively. Then, cells were incubated with 50 nM diAcFAM HaloTag ligand (488 nm, Promega) and 1 $\mu\text{g}/\text{ml}$ doxycycline for 45 min to label presynthesized Xist RNA molecules, before washing with medium containing 1 $\mu\text{g}/\text{ml}$ doxycycline for 15 min. Next, the different coverslips were incubated with 50 nM JF-585 HaloTag ligand and 1 $\mu\text{g}/\text{ml}$ doxycycline for 10, 20, 30, 40, 50, and 60 min, respectively, to label newly synthesized Xist RNA molecules, before being washed with PBS. Induction and staining times with the first HaloTag ligand were staggered, such that all coverslips could be fixed at the same time despite the different staining times with the second HaloTag ligand.

Xist turnover on chromatin

For assessing the turnover of Xist RNA, cells grown on precision coverslips were stained with 50 nM diAcFAM HaloTag ligand after 1.5 or 24 hours doxycycline induction, respectively, as described above. After the first pulse, coverslips were incubated with 50 nM JF-585 HaloTag ligand and 1 $\mu\text{g}/\text{ml}$ doxycycline for 60, 80, 100, 120, 140, 160, 180, 200, and 220 min, respectively, to label newly synthesized Xist RNA molecules, while one coverslip per experiment was not stained with the second HaloTag ligand at all and served as 0 min time point. Coverslips were finally washed with PBS. Induction and staining times with the first HaloTag ligand were staggered, such that all coverslips could be fixed at the same time despite the different staining times with the second HaloTag ligand. For each experiment, the endpoint was determined as when signal from the first HaloTag ligand could no longer be detected in the cells for two time points in a row.

Image analysis workflow

Reconstructed 3D-SIM image stacks were pre-processed and subjected to modulation contrast filtering as described above (36). Thereafter, conservative manual thresholding of the red and green channel was performed to discard background signal originating from free diffusing fluorescent BglG-Halo and thus prevent detection of false-positive signals. Lateral color channel alignment was performed as described above. The resulting images were used as representative images of whole nuclei. For fur-

ther analysis however, the DAPI channel was discarded, and Xist territories were cropped manually using Fiji to exclude signal from BglG-Halo accumulation in the nucleoli, or signal from other cells. The cropped dimensions were later used to define Xist territory volume during expansion and steady state in all different cell types.

To assess the difference in fluorescence intensity originating from the Xist territory as compared with the BglG-Halo fusion protein in nucleoplasm, we determined the intensity fold change of the average fluorescence signal intensity of segmented foci (using the *makefile* script described below for the determination of centroid positions) within the cropped Xist territory as compared with segmented background foci in a same sized nuclear volume outside the Xist territory (36). For this analysis manual thresholding was not performed so as to capture fluorescence background foci from free BglG fusion proteins. Similarly, we assessed how many CIZ1 molecules bind to each Xist molecule by measuring the average fluorescence intensity of the CIZ1 immunofluorescence foci within the Xist territory and in a corresponding volume of the nucleus outside the Xist territory.

The processed RNA-SPLIT image files were analyzed using an in-house adapted *makefile* script for masking of the signal and centroid determination by watershed algorithm, which also allowed for the determination and comparison of the intensities of different Xist foci (36). The output data were used to determine the number of Xist foci during expansion and steady state phase in all different cell types. Moreover, they were used to determine the transcription rates on the basis of the centroid count of the HaloTag ligand labeling newly synthesized Xist RNA molecules, as well as the turnover of Xist RNA on the basis of the count of the HaloTag ligand labeling presynthesized Xist RNA molecules.

NNA and variations thereof were conducted on the basis of the x, y, and z coordinates of centroids determined previously using a different in-house adapted *makefile* script (36). Distances determined from HaloTag ligand labeling newly synthesized RNA to the HaloTag ligand labeling presynthesized RNA were used to assess pairing behavior of Xist RNA during expansion and steady state in all cell types. Data from female C127 cells pulsed with EdU used previously for alignment were used as a technical control to determine nearest neighbor distances of molecules labeled with different ligands at the same time. Here, only EdU files acquired on the days of corresponding RNA-SPLIT data acquisition were used, allowing for sample-specific matched technical controls. Additionally, "Random" sample controls were generated in a sample-specific manner by scrambling of the x, y and z coordinates of

the centroids determined for newly synthesized RNA of each specific sample using Microsoft Excel.

Using a variation of the aforementioned NNA, median distances between each molecule and its ten nearest neighboring molecules in the same channel were determined as a measure of Xist RNA density. Combined densities of newly synthesized and presynthesized RNA in expansion and steady state were used for comparison of Xist RNA densities in different cell types. For NPCs in particular, median distances between each molecule and all other molecules were determined as measure of Xist RNA density to account for widespread distribution of Xist RNA throughout the nucleus in *Ciz1* KO NPCs.

Approximate localizations of the Xist transcription site were determined for each Xist territory on the basis of fluorescence intensity and density of the newly synthesized Xist RNA signal of WT mESCs. A variation of NNA was used to measure the distance of said approximate transcription site to all newly synthesized Xist molecules and to all presynthesized Xist molecules separately. To account for variability in Xist territory size, distances were normalized to the maximum distance measured for each territory, which was set to 1. This was then used to characterize the spreading behavior of newly synthesized Xist RNA molecules by comparing distance distributions in relation to the transcription site over time. Here, the Xist territory was divided into 3 zones, with zone 1, 2, and 3 extending 0 to 50%, 50 to 75%, and 75 to 100% of the maximum distance from the transcription site, respectively. Then, the proportion of newly synthesized or presynthesized Xist RNA molecules in each zone over time was quantified. This approach allowed for the time-resolved comparison of newly synthesized Xist RNA molecule and presynthesized Xist RNA molecule distributions during both expansion and steady state in WT mESCs. A rate of expansion could be calculated, because NNA distances were measured in 3D and the 3D volumes of the Xist territories were already known. On average, Xist territories had a size of 98.9 μm^3 in expansion, which can be set equal to 100% of the normalized volume used to determine Xist spreading previously. On average, newly synthesized Xist extends across 29.9% of this volume after 20 min and 35.2% after 60 min, meaning that there is an increase of 5.3% of the Xist expansion volume within 40 min. 5.3% of the average Xist territory volume of 98.9 μm^3 corresponds to 5.1 μm^3 . Based on this, the expansion rate of newly synthesized Xist RNA can be approximated as 7.7 $\mu\text{m}^3/\text{hour}$. Furthermore, the localizations of transcription sites could be used to assess their distribution during expansion as compared with steady state phase. Here, 3D coordinates

of Xist transcription sites were normalized to Xist territory dimensions and Xist territories were divided into three zones to account for variability in Xist territory size.

Dual-color control

To exclude that the results obtained by NNA are result from simultaneous labeling of Xist RNA molecules with BglG-Halo fusion proteins labeled with the two different HaloTag ligands, a dual-color control was performed. A total of six coverslips with WT mESCs were induced for 24 hours with 1 µg/ml doxycycline, before being incubated with medium containing 50 nM diAcFAM HaloTag ligand (488 nm, Promega), 50 nM JF-585 HaloTag ligand and 1 µg/ml doxycycline for 45 min. Then, coverslips were washed with medium containing 1 µg/ml doxycycline for 15 min, followed by a wash with PBS and preparation for imaging as described previously.

Dox washout experiment

To assess the turnover on chromatin of Xist RNA when Xist transcription is reduced, a washout of doxycycline was performed. Here, 10 coverslips with cells were sequentially stained with two different HaloTag ligands. WT mESCs were induced for 1.5 hours with 1 µg/ml doxycycline. Cells were then incubated with medium containing 50 nM diAcFAM HaloTag ligand (488 nm, Promega) but without doxycycline for 45 min to label presynthesized Xist RNA molecules, before washing just with medium for 15 min. Next, the different coverslips were incubated with 50 nM JF-585 HaloTag ligand but without doxycycline for 60, 80, 100, 120, 140, 160, 180, 200, and 220 min, respectively, to label newly synthesized Xist RNA molecules, while one coverslip was not stained with the second HaloTag ligand and served as the 0 min time point. Coverslips were washed with PBS and samples were prepared for imaging as described previously. Induction and staining times with the first HaloTag ligand were staggered, such that all coverslips could be fixed at the same time despite the different staining times with the second HaloTag ligand. Successful reduction of Xist transcription was determined by comparison of the newly synthesized Xist RNA molecule count determined for the doxycycline washout experiment to that determined for WT mESCs during expansion.

SLAM-seq

Sample preparation

SLAM-seq of WT cells, as well as the corresponding parental cell line with untagged Xist, was performed using the SLAMseq Kinetics Kit, Catabolic Kinetics Module (cat. no. 062.24, Lexogen). Cells were grown in gelatin-coated 6-well plates after preplating to discard feeder cells, with 6 wells needed for each

experimental replica. When reaching 60 to 70% confluency, cells were induced with 1 µg/ml doxycycline for 17.5 to 20 hours depending on the length of the subsequent washout times. Then, transcribed RNA was labeled with 4SU by incubation with medium containing 500 µM 4SU (Lexogen) and 1 µg/ml doxycycline for 4 hours. Next, 4SU was withdrawn by washout for all samples except the 0 min sample. Different samples were washed with medium containing 1 µg/ml doxycycline and 50 mM uridine (in excess, Lexogen) for 30, 60, 90, 120, and 150 min, respectively. Induction, 4SU labeling, and withdrawal times were staggered, such that all samples could be harvested at the same time despite the different washout times. After cells were collected by centrifugation at 1500 g for 5 min in PBS, nuclear extracts were obtained as follows: Cells were washed again with PBS and resuspended in 10 volumes buffer A (10 mM HEPES pH 7.9, 1.5 mM MgCl₂, 10 mM KCl, 0.5 mM DTT and complete protease inhibitors in RNase free water). Subsequently cells were incubated on ice for 10 min and recovered by centrifugation, followed by resuspension in 3 volumes buffer A with 0.1% NP-40 for 10 min. Nuclei were recovered by centrifugation at and TRIzol/chloroform RNA extraction was performed using the SLAMseq Kinetics Kit (Lexogen). Then, samples were treated with Iodoacetamide to modify the 4-thiol group of S4U-containing nucleotides via the addition of a carboxyamidomethyl group using the SLAMseq Kinetics Kit (Lexogen). The RNA was precipitated and washed again, before being resuspended in nuclease free water. 1 ng RNA of each sample were run on the bioanalyzer to determine the exact RNA concentration and RNA integrity of all samples. Based on this, 1 µg RNA of each sample was then taken forward for library preparation using the Illumina TruSeq stranded total RNA kit (RS-122-2301). Quantification of the libraries was performed by quantitative PCR (qPCR) using KAPA Library Quantification DNA standards (Kapa Biosystems, KK4903). Finally, the libraries were pooled and 2 × 81 paired-end sequencing was performed using Illumina NextSeq500 (FC-404-2002).

Data analysis

Estimation of nuclear RNA half-life was performed using GRAND-SLAM (38). Briefly, the paired-end sequencing reads were mapped to mouse genome mm10 by STAR (v2.5.2b) (39) with the key parameters (-outFilterMultimapNmax 1-outFilterMismatchNmax 999-alignEndsType EndToEnd). Given that T to C conversion is the signature of SLAMseq, the T to C conversion rate was calculated as 4SU incorporation and the average of all the rest of the conversions was calculated as background due to errors from sequencing or library preparation. The

T to C conversion rate and background rate were calculated accordingly for each sample. The nuclear RNA decay was assumed to follow an exponential model, so the T2C conversion rate (or T2C conversion rate-corresponding background rate) was fitted to the exponential model to estimate the RNA's nuclear half-life. In addition, the sample (dox-treated A11B2 cells, ChrRNA-seq) (27) without 4SU incorporation was used to estimate the background mutation rate for all 12 potential mismatches. Half-life of Xist RNA and another nuclear lncRNA Pvt1 were plotted.

ChrRNA-seq

Sample preparation

For ChrRNA-seq experiments, cells were grown in gelatin-coated T25 flasks with feeder cells. When confluent, cells were preplated for 40 min twice to discard the feeder cells, and expanded to gelatin-coated 15 cm dishes. Before chromatin RNA extraction, cells were induced for 3 or 24 hours with 1 µg/ml doxycycline for expansion and steady state, respectively. A control sample comprising cells without addition of doxycycline was included with the analysis of each cell line. Chromatin RNA for each sequencing replica was extracted from one confluent 15 cm dish of cells. Cells were harvested and recovered by centrifugation at 1000 rpm for 3 min at room temperature, before being snap frozen on dry ice. Next, pellets were resuspended in RLB (10 mM Tris pH 7.5, 10 mM KCl, 1.5 mM MgCl₂, and 0.1% NP40) and incubated on ice for 5 min to lyse the cells. Nuclei were purified by centrifugation through a sucrose cushion (24% sucrose in RLB) at 2800 g for 10 min at 4°C. The pellets were resuspended in NUN1 (20 mM Tris pH 7.5, 75 mM NaCl, 0.5 mM EDTA, 50% glycerol), and subsequently lysed with NUN2 (20 mM HEPES pH 7.9, 300 mM NaCl, 7.5 mM MgCl₂, 0.2 mM EDTA, 1 M urea). Samples were incubated for 15 min on ice, vortexing occasionally, before being centrifuged at 2800 g for 10 min at 4°C to isolate the insoluble chromatin fraction. The pellets were resuspended in TRIzol and homogenized by passing multiple times through a 23-gauge needle. Finally, chromatin-associated RNA was purified through standard TRIzol/chloroform extraction followed by isopropanol precipitation. Samples were treated with Turbo DNase and the RNA was purified by RNeasy column cleanup (Qiagen). 100 ng - 1 µg RNA of each sample were taken forward for library preparation using the Illumina TruSeq stranded total RNA kit (RS-122-2301). Quantification of the libraries was performed by qPCR with KAPA Library Quantification DNA standards (Kapa Biosystems, KK4903). Finally, the libraries were pooled and 2 × 81 paired-end sequencing was performed using Illumina NextSeq500 (FC-404-2002).

Data analysis

The analysis strategy that was used for ChrRNA-seq has been described in detail (27). In brief, raw fastq files of read pairs were mapped to an rRNA build by bowtie2 (v2.3.2), and rRNA-mapped reads were discarded. Remaining unmapped reads were aligned to the “N-masked” genome (from mm10 coordinates) with STAR (v2.4.2a) using parameters “-outFilterMultimapNmax 1 -outFilterMismatchNmax 4 -alignEndsType EndToEnd”. Unique alignments were retained for further analysis. 23,005,850 single-nucleotide polymorphism (SNPs) between Cast and 129S genomes identified previously (40), were used for allelic split. These were used to split the alignment into distinct alleles (Cast and 129S) with the help of SNPsplit (v0.2.0; Babraham Institute, Cambridge, UK). The allelic read numbers were counted using the program featureCounts (-t transcript -g gene_id -s 2) (41), whereas the alignments were sorted by Samtools (42). For biallelic analysis, counts were normalized to one million mapped read pairs using the edgeR R package. Genes with a minimum of 10 SNP-covering reads across all the samples were further taken to calculate the allelic ratio of Xi/(Xi+Xa). Here, Xi and Xa indicate the inactive and active allele, respectively. Xist mediated gene silencing during expansion and steady state was determined by the difference in the aforementioned allelic ratios between uninduced and doxycycline induced samples.

ChIP-seq

ES tissue culture

Biological replicate clones for SPEN^{ARRM} and SPEN^{SPOCmut} were derived from iXist-Chr X cells. ES cells cultured on feeders were preplated for 30 min, then plated on 15-cm dishes. Xist was induced by addition of 1 µg/ml doxycycline to growth media 3 hours or 24 hours before harvesting cells. Whereas all samples for the 3 hours experiment were processed in parallel on the same day, for the 24 hours experiment the SPEN^{ARRM} lines, SPEN^{SPOCmut} cell lines, and each of the three replicates of iXist-Chr X (WT) cells were processed on separate occasions.

Native ChIP-seq

H2AK119ub1 native ChIP-seq was performed for iXist-Chr X, SPEN^{ARRM} and SPEN^{SPOCmut} ES cell lines largely as previously described (27) using buffers supplemented with 10 mM of the deubiquitinase inhibitor N-ethylmaleimide (Sigma, E3876-5G) throughout. Briefly, 50 × 10⁶ ES cells were lysed in RSB (10 mM Tris pH 8, 10 mM NaCl, 3 mM MgCl₂, 0.1% NP40) for 5 min on ice with gentle inversion. Nuclei were resuspended in 1 ml of RSB + 0.25 M sucrose + 3 mM CaCl₂, treated with 200 U of MNase (Fermentas) for 5 min at 37°C,

quenched with 4 µl of 1 M EDTA, then centrifuged at 5000 rpm for 5 min. The supernatant was transferred to a fresh tube as fraction S1. The chromatin pellet was incubated for 1 hour in 300 µl of nucleosome release buffer (10 mM Tris pH 7.5, 10 mM NaCl, 0.2 mM EDTA), carefully passed five times through a 27G needle, and then centrifuged at 5000 rpm for 5 min. The supernatant from this S2 fraction was combined with S1 as soluble chromatin extract. For each ChIP reaction, 100 µl of chromatin was diluted in Native ChIP incubation buffer (10 mM Tris pH 7.5, 70 mM NaCl, 2 mM MgCl₂, 2 mM EDTA, 0.1% Triton) to 1 ml and incubated with 4 µl H2AK119ub1 Ab (Cell Signaling Technology, #8240) overnight at 4°C. Samples were incubated for 1 hour with 40 µl protein A agarose beads preblocked in Native ChIP incubation buffer with 1 mg/ml BSA and 1 mg/ml yeast tRNA, then washed for a total of four times in Native ChIP wash buffer (20 mM Tris pH 7.5, 2 mM EDTA, 125 mM NaCl, 0.1% Triton) and once in TE. The DNA was eluted with 1% SDS and 100 mM NaHCO₃, and was purified using the ChIP DNA Clean and Concentrator kit (Zymo Research). 50 ng of ChIP DNA was used for library prep using the NEBNext Ultra II DNA Library Prep Kit with NEBNext Single indices (E7645), and then quantified using a Bioanalyzer 2100 (Agilent) and a Qubit fluorometer (Invitrogen). The libraries were pooled and 2 × 81 paired-end sequencing was performed using Illumina NextSeq500 (FC-404-2002).

Native ChIP-seq data analysis

Raw fastq read pairs were mapped to the “N-masked” mm10 genome by bowtie2 (v2.2.6) using parameters “-very-sensitive-no-discordant-no-mixed -X 2000”. Alignment files were subsequently filtered to remove unmapped read pairs and PCR duplicates (picard-tools MarkDuplicates). For allelic analysis, we made use of SNPs between Cast and 129S genomes and used SNPsplit (v0.2.0; Babraham Institute, Cambridge, UK) to split 55 to 60% of filtered alignments into distinct alleles (Cast and 129S) using the parameter “-paired”. Each alignment file was then processed into bedGraph format by genomeCoverageBed [BEDtools (43)] and normalized to the total library size of the sample. The custom script ExtractInfoFrombedGraph_AtBed.py (<https://github.com/guifengwei>) was used to extract values of H2AK119ub1 enrichment for 250 kb windows spanning the whole Chr X (Fig. 5) or the 103.5 Mb region of Chr X proximal to Xist (fig. S10). Gain of H2AK119ub1 upon Xist expression was calculated by subtraction of uninduced from 24 or 3 hours induced samples (Dox - NoDox). Line plots were generated in R from replicates averaged for each mutant (3x iXist-Chr X technical replicates, 2x SPEN^{ARRM} clones, 2x SPEN^{SPOCmut} clones).

Western blot

For CIZ1 Western blot experiments, the candidate KO clones, and WT cells serving as control, were grown in gelatin-coated T25 flasks each with feeder cells. When confluent, cells were preplated for 40 min twice to discard the feeder cells, and subsequently plated in a well of a gelatin-coated 6-well plate each. When confluent, cells were washed with PBS and detached using TrypLE Express (Thermo Fisher Scientific). Cells were washed and recovered by centrifugation, before 3 × 10⁶ cells of each clone were dissolved in 200 µl 2x SMASH buffer [33 mM Tris-HCl (pH 6.8), 11% Glycerol, 40 mg/ml SDS, 200 µg/ml bromophenol blue and 10% β-mercaptoethanol in nuclease-free water]. Samples were left shaking for 20 min, and then snap frozen on dry ice and thawed once. Samples were then separated by SDS polyacrylamide gel electrophoresis (8% separating gel and 5% stacking gel) at 80 V for 15 min, and then at 180 V for another 70 min. Next, samples were transferred onto a PVDF membrane by semidry transfer at 15 V for 1 hour. The membrane was blocked by incubation with 10 ml PBS, 0.1% Tween (PBST) with 5% w/v Marvel milk powder for 1 hour at room temperature. The membrane was then incubated with the corresponding primary antibody [CIZ1, anti-rabbit, affinity purified, polyclonal (from the Coverley laboratory, University of York); and tubulin, anti-rabbit, Cell Signaling, cat. no 2144] diluted 1:1000 in PBST with 5% w/v Marvel milk powder at 4°C overnight. The membrane was washed three times in PBST with 5% w/v Marvel milk powder for 10 min each, before being incubated with secondary antibody conjugated to horseradish peroxidase (anti-rabbit, HRP linked, Amersham) diluted 1:1000 in PBST with 5% w/v Marvel milk powder for 1 hour. After washes with PBST with 5% w/v Marvel milk powder and finally with PBST followed by PBS only, bands were visualized using ECL (GE Healthcare) for antibody detection.

Southern blot

For Southern blot analysis of candidate SPEN^{ARRM} clones, cells were grown in gelatin-coated T25 flasks each with feeder cells. When confluent, cells were preplated for 40 min twice to discard the feeder cells, and subsequently plated in a well of a gelatin-coated 6-well plate each. Cells were washed three times with PBS, before 1 ml lysis buffer (10 mM NaCl, 10 mM Tris pH 7.5, 10 mM EDTA pH 8, 0.5% sarcosyl; filter sterilized; 1 mg/ml Proteinase K added fresh) was added directly to each well to lyse the cells completely. Lysates were incubated at 55°C shaking at 300 rpm overnight. Standard phenol chloroform extraction of the DNA was carried out using MaXtract High Density tubes (Qiagen). DNA was precipitated with NaCl and EtOH and the DNA was

recovered by were centrifugation. Next, an EcoRV restriction digest of the samples was performed and 5 µg digested DNA each were run on a 1% EtBr agarose gel for ~4 hours at 50 V. The gel was incubated with deperunation solution (0.125 M HCl in Milli-Q water) and for 15 min, with denaturation buffer (0.5 M NaOH, 1.5 M NaCl in Milli-Q water) for 45 min and finally with neutralization buffer (0.5 M Tris, 1.5 M NaCl in Milli-Q water, pH 8) for 30 min. After capillary transfer overnight to an Immobilon NY+ membrane (Millipore) for at least 18 hours, the membrane was air dried and ultraviolet (UV) cross-linked using the Stratelinker.

The membrane prehybridized with Dextran - SLS - SCC hybridization solution prewarmed to 65°C (83 mg/ml dextran sulfate, 5x SSC and 0.875% N-lauryl sarcosine sodium salt solution in Milli-Q water filtered through a 0.8 µm membrane before addition of 48 µg/ml denatured sheared salmon sperm DNA just before use) for 1 hour at 65°C. The probe was prepared using the prime-H II kit (Stratagene) as follows from a 626 bp fragment downstream of the sgRNA used for the SPEN^{ARRM} in exon 12 (table S1). The probe was purified using a G50 Micro column (GE Healthcare), before being boiled for 5 min at 95°C. The denatured probe was placed on ice for 1 min, added to the hybridization mixture and membrane, and then hybridized overnight at 65° to 67°C. The next day, the membrane was washed twice with low stringency at 65°C for 15 min each. It was subsequently exposed in a Fuji cassette overnight, before it was scanned on a FLA-7000 (Fujifilm). Mutant bands were detectable at 2.64 kb, whereas WT bands were detectable at 4 kb.

Statistical analysis

For the comparison of two independent large datasets throughout the project, statistical significance was determined by conducting an unpaired two-sample Wilcoxon test using R. This statistical test determines whether it is equally likely that a randomly selected value from one dataset will be less than or greater than a randomly chosen value from another population, making it ideal to determine whether two large datasets have the same distribution. Hence, the unpaired two-sample Wilcoxon test was used as a nonparametric alternative to the unpaired *t* test to determine statistical significance.

REFERENCES AND NOTES

- J. A. Graves, Evolution of vertebrate sex chromosomes and dosage compensation. *Nat. Rev. Genet.* **17**, 33–46 (2016). doi: [10.1038/nrg.2015.2](https://doi.org/10.1038/nrg.2015.2); PMID: [26616198](https://pubmed.ncbi.nlm.nih.gov/26616198/)
- I. Pinheiro, E. Heard, X chromosome inactivation: New players in the initiation of gene silencing. *F1000 Res.* **6**, 344 (2017). doi: [10.12688/f1000research.10707.1](https://doi.org/10.12688/f1000research.10707.1); PMID: [28408975](https://pubmed.ncbi.nlm.nih.gov/28408975/)
- J. T. Lee, R. Jaenisch, Long-range cis effects of ectopic X-inactivation centres on a mouse autosome. *Nature* **386**, 275–279 (1997). doi: [10.1038/386275a0](https://doi.org/10.1038/386275a0); PMID: [9069285](https://pubmed.ncbi.nlm.nih.gov/9069285/)
- A. Wutz, R. Jaenisch, A shift from reversible to irreversible X inactivation is triggered during ES cell differentiation. *Mol. Cell* **5**, 695–705 (2000). doi: [10.1016/S1097-2765\(00\)80248-8](https://doi.org/10.1016/S1097-2765(00)80248-8); PMID: [10882105](https://pubmed.ncbi.nlm.nih.gov/10882105/)
- S. M. Duthie *et al.*, Xist RNA exhibits a banded localization on the inactive X chromosome and is excluded from autosomal material in cis. *Hum. Mol. Genet.* **8**, 195–204 (1999). doi: [10.1093/hmg/8.2.195](https://doi.org/10.1093/hmg/8.2.195); PMID: [9931327](https://pubmed.ncbi.nlm.nih.gov/9931327/)
- C. M. Clemson, J. A. McNeil, H. F. Willard, J. B. Lawrence, Xist RNA paints the inactive X chromosome at interphase: Evidence for a novel RNA involved in nuclear/chromosome structure. *J. Cell Biol.* **132**, 259–275 (1996). doi: [10.1083/jcb.132.3.259](https://doi.org/10.1083/jcb.132.3.259); PMID: [8636206](https://pubmed.ncbi.nlm.nih.gov/8636206/)
- Y. Hasegawa *et al.*, The matrix protein hnRNP U is required for chromosomal localization of Xist RNA. *Dev. Cell* **19**, 469–476 (2010). doi: [10.1016/j.devcel.2010.08.006](https://doi.org/10.1016/j.devcel.2010.08.006); PMID: [20833368](https://pubmed.ncbi.nlm.nih.gov/20833368/)
- C. Chu *et al.*, Systematic discovery of Xist RNA binding proteins. *Cell* **161**, 404–416 (2015). doi: [10.1016/j.cell.2015.03.025](https://doi.org/10.1016/j.cell.2015.03.025); PMID: [25843628](https://pubmed.ncbi.nlm.nih.gov/25843628/)
- R. Ridings-Figueroa *et al.*, The nuclear matrix protein CIZ1 facilitates localization of Xist RNA to the inactive X-chromosome territory. *Genes Dev.* **31**, 876–888 (2017). doi: [10.1101/gad.295907.117](https://doi.org/10.1101/gad.295907.117); PMID: [28546514](https://pubmed.ncbi.nlm.nih.gov/28546514/)
- H. Sunwoo, D. Colognori, J. E. Froberg, Y. Jeon, J. T. Lee, Repeat E anchors Xist RNA to the inactive X chromosomal compartment through CDKN1A-interacting protein (CIZ1). *Proc. Natl. Acad. Sci. U.S.A.* **114**, 10654–10659 (2017). doi: [10.1073/pnas.1711206114](https://doi.org/10.1073/pnas.1711206114); PMID: [28923964](https://pubmed.ncbi.nlm.nih.gov/28923964/)
- D. Smeets *et al.*, Three-dimensional super-resolution microscopy of the inactive X chromosome territory reveals a collapse of its active nuclear compartment harboring distinct Xist RNA foci. *Epigenetics Chromatin* **7**, 8 (2014). doi: [10.1186/1756-8935-7-8](https://doi.org/10.1186/1756-8935-7-8); PMID: [25057298](https://pubmed.ncbi.nlm.nih.gov/25057298/)
- J. M. Engreitz *et al.*, RNA-RNA interactions enable specific targeting of noncoding RNAs to nascent Pre-mRNAs and chromatin sites. *Cell* **159**, 188–199 (2014). doi: [10.1016/j.cell.2014.08.018](https://doi.org/10.1016/j.cell.2014.08.018); PMID: [25259926](https://pubmed.ncbi.nlm.nih.gov/25259926/)
- J. M. Engreitz *et al.*, The Xist lncRNA exploits three-dimensional genome architecture to spread across the X chromosome. *Science* **341**, 1237973 (2013). doi: [10.1126/science.1237973](https://doi.org/10.1126/science.1237973); PMID: [23828888](https://pubmed.ncbi.nlm.nih.gov/23828888/)
- N. Brockdorff, Localized accumulation of Xist RNA in X chromosome inactivation. *Open Biol.* **9**, 190213 (2019). doi: [10.1098/rsob.190213](https://doi.org/10.1098/rsob.190213); PMID: [31795917](https://pubmed.ncbi.nlm.nih.gov/31795917/)
- K. Ng *et al.*, A system for imaging the regulatory noncoding Xist RNA in living mouse embryonic stem cells. *Mol. Biol. Cell* **22**, 2634–2645 (2011). doi: [10.1091/mbc.e11-02-0146](https://doi.org/10.1091/mbc.e11-02-0146); PMID: [21613549](https://pubmed.ncbi.nlm.nih.gov/21613549/)
- N. Ha *et al.*, Live-cell Imaging and functional dissection of Xist RNA reveal mechanisms of X chromosome inactivation and reactivation. *iScience* **8**, 1–14 (2018). doi: [10.1016/j.isci.2018.09.007](https://doi.org/10.1016/j.isci.2018.09.007); PMID: [30266032](https://pubmed.ncbi.nlm.nih.gov/30266032/)
- B. Moindroit *et al.*, A pooled shRNA screen identifies Rbm15, Spen, and Wtap as factors required for Xist RNA-mediated silencing. *Cell Rep.* **12**, 562–572 (2015). doi: [10.1016/j.celrep.2015.06.053](https://doi.org/10.1016/j.celrep.2015.06.053); PMID: [26190105](https://pubmed.ncbi.nlm.nih.gov/26190105/)
- Y. Markaki *et al.*, Xist-seeded nucleation sites form local concentration gradients of silencing proteins to inactivate the X-chromosome. bioRxiv 2020.11.22.393546 [Preprint]. 23 November 2020. <https://doi.org/10.1101/2020.11.22.393546>
- V. A. Herzog *et al.*, Thiol-linked alkylation of RNA to assess expression dynamics. *Nat. Methods* **14**, 1198–1204 (2017). doi: [10.1038/nmeth.4435](https://doi.org/10.1038/nmeth.4435); PMID: [28945705](https://pubmed.ncbi.nlm.nih.gov/28945705/)
- M. D. Simon *et al.*, High-resolution Xist binding maps reveal two-step spreading during X-chromosome inactivation. *Nature* **504**, 465–469 (2013). doi: [10.1038/nature12719](https://doi.org/10.1038/nature12719); PMID: [24162848](https://pubmed.ncbi.nlm.nih.gov/24162848/)
- F. Kraus *et al.*, Quantitative 3D structured illumination microscopy of nuclear structures. *Nat. Protoc.* **12**, 1011–1028 (2017). doi: [10.1038/nprot.2017.020](https://doi.org/10.1038/nprot.2017.020); PMID: [28406495](https://pubmed.ncbi.nlm.nih.gov/28406495/)
- A. Monfort *et al.*, Identification of Spen as a crucial factor for Xist function through forward genetic screening in haploid embryonic stem cells. *Cell Rep.* **12**, 554–561 (2015). doi: [10.1016/j.celrep.2015.06.067](https://doi.org/10.1016/j.celrep.2015.06.067); PMID: [26190100](https://pubmed.ncbi.nlm.nih.gov/26190100/)
- Z. Lu *et al.*, RNA duplex map in living cells reveals higher-order transcriptome structure. *Cell* **165**, 1267–1279 (2016). doi: [10.1016/j.cell.2016.04.028](https://doi.org/10.1016/j.cell.2016.04.028); PMID: [27180905](https://pubmed.ncbi.nlm.nih.gov/27180905/)
- C. A. McHugh *et al.*, The Xist lncRNA interacts directly with SHARP to silence transcription through HDAC3. *Nature* **521**, 232–236 (2015). doi: [10.1038/nature14443](https://doi.org/10.1038/nature14443); PMID: [25915022](https://pubmed.ncbi.nlm.nih.gov/25915022/)
- J. J. Zyllicz *et al.*, The implication of early chromatin changes in X chromosome inactivation. *Cell* **176**, 182–197.e23 (2019). doi: [10.1016/j.cell.2018.11.041](https://doi.org/10.1016/j.cell.2018.11.041); PMID: [30595450](https://pubmed.ncbi.nlm.nih.gov/30595450/)
- F. Dossin *et al.*, SPEN integrates transcriptional and epigenetic control of X-inactivation. *Nature* **578**, 455–460 (2020). doi: [10.1038/s41586-020-1974-9](https://doi.org/10.1038/s41586-020-1974-9); PMID: [32025035](https://pubmed.ncbi.nlm.nih.gov/32025035/)
- T. B. Nesterova *et al.*, Systematic allelic analysis defines the interplay of key pathways in X chromosome inactivation. *Nat. Commun.* **10**, 3129 (2019). doi: [10.1038/s41467-019-11171-3](https://doi.org/10.1038/s41467-019-11171-3); PMID: [31311937](https://pubmed.ncbi.nlm.nih.gov/31311937/)
- A. Wutz, T. P. Rasmussen, R. Jaenisch, Chromosomal silencing and localization are mediated by different domains of Xist RNA. *Nat. Genet.* **30**, 167–174 (2002). doi: [10.1038/ng820](https://doi.org/10.1038/ng820); PMID: [11780141](https://pubmed.ncbi.nlm.nih.gov/11780141/)
- M. Ariyoshi, J. W. R. Schwabe, A conserved structural motif reveals the essential transcriptional repression function of Spen proteins and their role in developmental signaling. *Genes Dev.* **17**, 1909–1920 (2003). doi: [10.1101/gad.266203](https://doi.org/10.1101/gad.266203); PMID: [12897056](https://pubmed.ncbi.nlm.nih.gov/12897056/)
- E. Miron *et al.*, Chromatin arranges in chains of mesoscale domains with nanoscale functional topography independent of cohesin. *Sci. Adv.* **6**, eaba8811 (2020). doi: [10.1126/sciadv.aba8811](https://doi.org/10.1126/sciadv.aba8811); PMID: [32967822](https://pubmed.ncbi.nlm.nih.gov/32967822/)
- G. V. Los *et al.*, HaloTag: A novel protein labeling technology for cell imaging and protein analysis. *ACS Chem. Biol.* **3**, 373–382 (2008). doi: [10.1021/cb800025k](https://doi.org/10.1021/cb800025k); PMID: [18533659](https://pubmed.ncbi.nlm.nih.gov/18533659/)
- F. Oswald *et al.*, A phospho-dependent mechanism involving NCoR and KMT2D controls a permissive chromatin state at Notch target genes. *Nucleic Acids Res.* **44**, 4703–4720 (2016). doi: [10.1093/nar/gkw105](https://doi.org/10.1093/nar/gkw105); PMID: [26912830](https://pubmed.ncbi.nlm.nih.gov/26912830/)
- L. Conti *et al.*, Niche-independent symmetrical self-renewal of a mammalian tissue stem cell. *PLoS Biol.* **3**, e283 (2005). doi: [10.1371/journal.pbio.0030283](https://doi.org/10.1371/journal.pbio.0030283); PMID: [16086633](https://pubmed.ncbi.nlm.nih.gov/16086633/)
- E. Splinter *et al.*, The inactive X chromosome adopts a unique three-dimensional conformation that is dependent on Xist RNA. *Genes Dev.* **25**, 1371–1383 (2011). doi: [10.1101/gad.633311](https://doi.org/10.1101/gad.633311); PMID: [21690198](https://pubmed.ncbi.nlm.nih.gov/21690198/)
- G. Ball *et al.*, SIMcheck: A toolbox for successful super-resolution Structured Illumination Microscopy. *Sci. Rep.* **5**, 15915 (2015). doi: [10.1038/srep15915](https://doi.org/10.1038/srep15915); PMID: [26525406](https://pubmed.ncbi.nlm.nih.gov/26525406/)
- L. Rodermund *et al.*, makefile and scripts for: Time-resolved structured illumination microscopy reveals key principles of Xist RNA spreading. Zenodo (2021); <http://doi.org/10.5281/zenodo.4725861>
- A. Matsuda, L. Schermelleh, Y. Hirano, T. Haraguchi, Y. Hiraoka, Accurate and fiducial-marker-free correction for three-dimensional chromatic shift in biological fluorescence microscopy. *Sci. Rep.* **8**, 7583 (2018). doi: [10.1038/s41598-018-25922-7](https://doi.org/10.1038/s41598-018-25922-7); PMID: [29765093](https://pubmed.ncbi.nlm.nih.gov/29765093/)
- C. Jürges, L. Dölken, F. Erhard, Dissecting newly transcribed and old RNA using GRAND-SLAM. *Bioinformatics* **34**, i218–i226 (2018). doi: [10.1093/bioinformatics/bty256](https://doi.org/10.1093/bioinformatics/bty256); PMID: [29949974](https://pubmed.ncbi.nlm.nih.gov/29949974/)
- A. Dobin *et al.*, STAR: Ultrafast universal RNA-seq aligner. *Bioinformatics* **29**, 15–21 (2013). doi: [10.1093/bioinformatics/bts635](https://doi.org/10.1093/bioinformatics/bts635); PMID: [23104886](https://pubmed.ncbi.nlm.nih.gov/23104886/)
- G. Pintacuda *et al.*, hnRNPK Recruits PCGF3/5-PRC1 to the Xist RNA B-Repeat to Establish Polycomb-Mediated Chromosomal Silencing. *Mol. Cell* **68**, 955–969.e10 (2017). doi: [10.1016/j.molcel.2017.11.013](https://doi.org/10.1016/j.molcel.2017.11.013); PMID: [29220657](https://pubmed.ncbi.nlm.nih.gov/29220657/)
- Y. Liao, G. K. Smyth, W. Shi, featureCounts: An efficient general purpose program for assigning sequence reads to genomic features. *Bioinformatics* **30**, 923–930 (2014). doi: [10.1093/bioinformatics/btt656](https://doi.org/10.1093/bioinformatics/btt656); PMID: [24227677](https://pubmed.ncbi.nlm.nih.gov/24227677/)
- H. Li *et al.*, The Sequence Alignment/Map format and SAMtools. *Bioinformatics* **25**, 2078–2079 (2009). doi: [10.1093/bioinformatics/btp352](https://doi.org/10.1093/bioinformatics/btp352); PMID: [19505943](https://pubmed.ncbi.nlm.nih.gov/19505943/)
- A. R. Quinlan, I. M. Hall, BEDTools: A flexible suite of utilities for comparing genomic features. *Bioinformatics* **26**, 841–842 (2010). doi: [10.1093/bioinformatics/btq033](https://doi.org/10.1093/bioinformatics/btq033); PMID: [20110278](https://pubmed.ncbi.nlm.nih.gov/20110278/)

ACKNOWLEDGMENTS

We thank A. Williams for assistance with next-generation sequencing (NGS); L. Lavis for providing a range of HaloTag ligands; and D. Sherratt, University of Oxford, and A. Castello,

University of Oxford, for valuable discussions. **Funding:** This work was funded by grants to L.R. from the Medical Research Council UK (MR/K501256/1) and grants to N.B. from the Wellcome Trust (103768). Imaging was performed at the Micron Oxford Advanced Bioimaging Unit funded by a Wellcome Trust Strategic Award (091911 and 107457/Z/15/Z). **Author contributions:** N.B., L.S., H.C., and L.R. conceived experiments; L.R., H.C., J.B., B.R., and T.N. carried out experiments; N.B., L.S., L.R., and H.C. wrote the manuscript; L.R. and R.O. performed image processing and analysis; G.W., R.O., and L.R. ran computational analysis; and R.O. and D.M.S.P. provided computational scripts. **Competing interests:** The authors

declare no competing interests. **Data and materials availability:** All data, parameters, and scripts used are available for reproducing the results of this investigation. Raw and reconstructed 3D-SIM images were deposited to the Image Data Resource (<https://idr.openmicroscopy.org>) under accession no. idr0110. The programs required to run all scripts for RNA-SPLIT image processing and analysis are ImageJ (Fiji) distribution with SIMcheck, R, and Octave. Makefile and scripts are available on Zenodo (36). All the high-throughput sequencing data encompassing ChrRNA-seq, ChIP-seq, and SLAM-seq are deposited in GEO under accession no. GSE154568.

SUPPLEMENTARY MATERIALS

science.sciencemag.org/content/372/6547/eabe7500/suppl/DC1
Supplementary Text
Figs. S1 to S12
Tables S1 and S2
MDAR Reproducibility Checklist
Movies S1 and S2

[View/request a protocol for this paper from Bio-protocol.](#)

11 September 2020; accepted 7 May 2021
10.1126/science.abe7500

Time-resolved structured illumination microscopy reveals key principles of Xist RNA spreading

Lisa Rodermund, Heather Coker, Roel Oldenkamp, Guifeng Wei, Joseph Bowness, Bramman Rajkumar, Tatyana Nesterova, David Miguel Susano Pinto, Lothar Schermelleh and Neil Brockdorff

Science **372** (6547), eabe7500.
DOI: 10.1126/science.abe7500

Visualizing Xist RNA dynamics

The noncoding RNA Xist, which controls the process of X chromosome inactivation in mammals, accumulates and spreads over the chromosome from which it is transcribed. The underlying basis for this unusual behavior is poorly understood. Using a new imaging approach called RNA-SPLIT for time-resolved analysis of Xist RNA molecules at super-resolution, Rodermund *et al.* analyzed fundamental parameters of Xist RNA behavior in normal cells and after the perturbation of factors implicated in Xist RNA function. The authors provide new insights into the basis of Xist RNA localization and confinement within the territory of a single X chromosome.

Science, abe7500, this issue p. eabe7500

ARTICLE TOOLS

<http://science.sciencemag.org/content/372/6547/eabe7500>

SUPPLEMENTARY MATERIALS

<http://science.sciencemag.org/content/suppl/2021/06/09/372.6547.eabe7500.DC1>

REFERENCES

This article cites 41 articles, 8 of which you can access for free
<http://science.sciencemag.org/content/372/6547/eabe7500#BIBL>

PERMISSIONS

<http://www.sciencemag.org/help/reprints-and-permissions>

Use of this article is subject to the [Terms of Service](#)

Science (print ISSN 0036-8075; online ISSN 1095-9203) is published by the American Association for the Advancement of Science, 1200 New York Avenue NW, Washington, DC 20005. The title *Science* is a registered trademark of AAAS.

Copyright © 2021 The Authors, some rights reserved; exclusive licensee American Association for the Advancement of Science. No claim to original U.S. Government Works